



# **NAVAL POSTGRADUATE SCHOOL**

**MONTEREY, CALIFORNIA**

## **THESIS**

**BREAKING WAVE TURBULENCE IN THE SURF ZONE**

by

Margaret E. Sweeny

June 2005

Thesis Advisor:  
Second Reader:

Timothy P. Stanton  
Edward B. Thornton

**Approved for public release; distribution is unlimited**

THIS PAGE INTENTIONALLY LEFT BLANK

<b>REPORT DOCUMENTATION PAGE</b>			<i>Form Approved OMB No. 0704-0188</i>	
Public reporting burden for this collection of information is estimated to average 1 hour per response, including the time for reviewing instruction, searching existing data sources, gathering and maintaining the data needed, and completing and reviewing the collection of information. Send comments regarding this burden estimate or any other aspect of this collection of information, including suggestions for reducing this burden, to Washington headquarters Services, Directorate for Information Operations and Reports, 1215 Jefferson Davis Highway, Suite 1204, Arlington, VA 22202-4302, and to the Office of Management and Budget, Paperwork Reduction Project (0704-0188) Washington DC 20503.				
<b>1. AGENCY USE ONLY (Leave blank)</b>		<b>2. REPORT DATE</b> June 2005	<b>3. REPORT TYPE AND DATES COVERED</b> Master's Thesis	
<b>4. TITLE AND SUBTITLE:</b> Breaking Wave Turbulence in the Surf Zone			<b>5. FUNDING NUMBERS</b>	
<b>6. AUTHOR(S)</b> Sweeny, Margaret E.				
<b>7. PERFORMING ORGANIZATION NAME(S) AND ADDRESS(ES)</b> Naval Postgraduate School Monterey, CA 93943-5000			<b>8. PERFORMING ORGANIZATION REPORT NUMBER</b>	
<b>9. SPONSORING /MONITORING AGENCY NAME(S) AND ADDRESS(ES)</b> N/A			<b>10. SPONSORING/MONITORING AGENCY REPORT NUMBER</b>	
<b>11. SUPPLEMENTARY NOTES</b> The views expressed in this thesis are those of the author and do not reflect the official policy or position of the Department of Defense or the U.S. Government.				
<b>12a. DISTRIBUTION / AVAILABILITY STATEMENT</b> Approved for public release; distribution is unlimited			<b>12b. DISTRIBUTION CODE</b>	
<b>13. ABSTRACT</b> <p>An increasingly exercised and precarious region of the maritime battlefield is the surf zone. Wave properties and turbulence dissipation from breaking waves in the surf zone were calculated from data collected during the 2001 RIPEX/ Steep Beach Experiment. Wave characteristics, such as current velocities, period, significant wave and sea surface height, and tide were examined. The tide was shown to have the major influence on the breadth and the location of the surf zone from the shoreline. Video imaging time series were geometrically transformed into plan views of pixel brightness related to wave breaking intensity. Surf zone boundaries were generated using both a computer algorithm and manual manipulation.</p> <p>Two methods were examined for calculating breaking wave dissipation rates for particularly robust days (110.5 -114.5). Velocity data were acquired using two electromagnetic current meters over the vertical mounted on a tower at mid-surf zone. The first method identified individual bores, which were ensemble averaged by phase over 30 minute records to obtain wave number spectra invoking Taylor's frozen turbulence hypothesis. Maximum dissipation rates underneath the bore cycle were shown to lag behind the sea surface elevation. The second method used 30 minute ensemble averaged spectra to obtain dissipation after Trowbridge and Elgar (2001). Dissipation rates calculated underneath each bore segment were orders of magnitude smaller when compared to the ensemble averaged technique.</p>				
<b>14. SUBJECT TERMS:</b> surf zone, turbulence, dissipation rate, breaking waves, image intensity			<b>15. NUMBER OF PAGES</b> 71	
			<b>16. PRICE CODE</b>	
<b>17. SECURITY CLASSIFICATION OF REPORT</b> Unclassified	<b>18. SECURITY CLASSIFICATION OF THIS PAGE</b> Unclassified	<b>19. SECURITY CLASSIFICATION OF ABSTRACT</b> Unclassified	<b>20. LIMITATION OF ABSTRACT</b> UL	

THIS PAGE INTENTIONALLY LEFT BLANK

**Approved for public release; distribution is unlimited.**

**BREAKING WAVE TURBULENCE IN THE SURF ZONE**

Margaret E. Sweeny  
Ensign, United States Navy  
B.S., United States Naval Academy, 2004

Submitted in partial fulfillment of the  
requirements for the degree of

**MASTER OF SCIENCE IN APPLIED SCIENCE  
(PHYSICAL OCEANOGRAPHY)**

from the

**NAVAL POSTGRADUATE SCHOOL  
June 2005**

Author: Margaret E. Sweeny

Approved by: Timothy P. Stanton  
Thesis Advisor

Edward B. Thornton  
Second Reader

Chairman Mary L. Batteen  
Chairman, Department of Oceanography

THIS PAGE INTENTIONALLY LEFT BLANK

## **ABSTRACT**

Wave properties and turbulence dissipation from breaking waves in the surf zone were calculated from data collected during the 2001 RIPEX/ Steep Beach Experiment. Wave characteristics, such as current velocities, period, significant wave and sea surface height, and tide were examined. The tide was shown to have the major influence on the breadth and the location of the surf zone from the shoreline. Video imaging time series were geometrically transformed into plan views of pixel brightness related to wave breaking intensity. Surf zone boundaries were generated using both a computer algorithm and manual manipulation.

Two methods were examined for calculating breaking wave dissipation rates for particularly robust days (110.5 -114.5). Velocity data were acquired using two electromagnetic current meters over the vertical mounted on a tower in mid-surf zone. The first method identified individual bores, which were ensemble averaged by phase over 30 minute records to obtain wave number spectra invoking Taylor's frozen turbulence hypothesis. Maximum dissipation rates underneath the bore cycle were shown to lag behind the sea surface elevation.

The second method used 30 minute ensemble averaged spectra to obtain dissipation after Trowbridge and Elgar (2001). Dissipation rates calculated underneath each bore segment were orders of magnitude smaller when compared to the ensemble averaged technique.

THIS PAGE INTENTIONALLY LEFT BLANK



# TABLE OF CONTENTS

<b>I.</b>	<b>INTRODUCTION.....</b>	<b>1</b>
<b>A.</b>	<b>NAVAL RELEVANCE .....</b>	<b>1</b>
<b>B.</b>	<b>AN OVERVIEW OF TURBULENCE.....</b>	<b>2</b>
<b>II.</b>	<b>RIPEX/STEEP BEACH EXPERIMENT .....</b>	<b>17</b>
<b>A.</b>	<b>OVERVIEW .....</b>	<b>17</b>
<b>B.</b>	<b>PHYSICAL EXPERIMENT.....</b>	<b>18</b>
<b>C.</b>	<b>INSTRUMENTS .....</b>	<b>19</b>
1.	Electromagnetic Current Meters.....	19
2.	BCDV .....	20
3.	Wave Wire .....	21
4.	Cameras .....	22
<b>III.</b>	<b>RESULTS .....</b>	<b>25</b>
<b>A.</b>	<b>IMAGE INTENSITY.....</b>	<b>25</b>
<b>B.</b>	<b>ENVIRONMENTAL DATA.....</b>	<b>28</b>
1.	Wave Direction.....	28
2.	Significant Wave Height.....	29
3.	Wave Period .....	29
4.	Tidal Cycle.....	31
<b>C.</b>	<b>BORE IDENTIFICATION .....</b>	<b>34</b>
<b>IV.</b>	<b>DISCUSSION .....</b>	<b>37</b>
<b>V.</b>	<b>CONCLUSIONS .....</b>	<b>49</b>
	<b>LIST OF REFERENCES.....</b>	<b>51</b>
	<b>INITIAL DISTRIBUTION LIST .....</b>	<b>53</b>

THIS PAGE INTENTIONALLY LEFT BLANK

## LIST OF FIGURES

Figure 1.	Turbulent eddies entrained within the water column by breaking waves homogenize the logarithmic current velocity profile to the depth at which the turbulence extends.....	3
Figure 2.	(From: Kundu, 1990). Logarithmic velocity distributions near smooth and rough surfaces .....	4
Figure 3.	(After: Faria et al., 1998). Results of the robust days depicted a logarithmic profile for the mean longshore currents. Depicted are the measured (asterisk) and predicted (line) vertical profiles, superposed on bottom profiles with mean surface sea elevation indicated by open circles and measured $C_f$ values.....	5
Figure 4.	(From: Faria et al, 1998). A diagram of the placement of alongshore and cross-shore instrument arrays in the Duck 94 Experiment. ....	6
Figure 5.	(From: Kundu, 1990). Two of the three regions of a wave's energy density spectra are depicted, the inertial subrange with its characteristic ( $-5/3$ ) slope and the dissipation range, where molecular viscosity begins to dominate the turbulent eddies ability to rotate.....	8
Figure 6.	(From: George et al., 1994). A frequency spectrum from a hotfilm time series showing the orbital wave ( $f^3$ ) slope and inertial subrange turbulent ( $f^{5/3}$ ) regimes.....	9
Figure 7.	(From: Thornton, 1979). Horizontal and surface elevation spectra, the left panel for plunging breakers and the right for spilling breakers.....	11
Figure 8.	The modifier $I\left(\frac{\sigma}{V}, \theta\right)$ , and the relationship between sigma/velocity and theta.....	14
Figure 9.	(From: Stanton T.P, 2002). The location of the vertical tower array situated within the surf zone and other sensors used in the RIPEX/STEEP BEACH experiment. The vertical tower instrument array is delineated as "Mast and Goal Post" or "M+G". ....	19
Figure 10.	Close up snap shot of the vertical tower array of current sensors deployed in the field during the RIPEX/STEEP BEACH experiment. On the left, Macroscopic kelp is visible hanging from two of the EM sensors. On the right, the vertical tower array and BCDV situated in the surf zone during the experiment as large waves break in the background.....	21
Figure 11.	(From: Stanton T.P and E. B. Thornton., 2002,a,b). A diagram of the vertical tower array of electromagnetic current and conductivity sensors and capacitance wave staff. Also depicted is the BCDV.....	22
Figure 12.	A raw snapshot image taken from the southern ELTEC camera April 22, 2001. The vertical tower array and BCDV are visible within the surf zone. Areas of intense wave breaking within the surf zone are indicated by the regions of brighter (whiter) pixel intensity .....	23
Figure 13.	A rectified image of the surf zone taken April 22, 2001. Dark shading indicate the location of rip currents within the surf zone where fewer	

	waves break in the deeper rip channel. The vertical instrument tower array is visible as the slightly skewed shaded line in the right panel.....	23
Figure 14.	Image intensity plot of day 113 (April 23, 2001). Both the computer algorithm for the lower bounds (black dots) and the upper bounds (white dots) are visible. Manual manipulations of the surf zone boundaries are indicated by the magenta boundary dots.....	26
Figure 15.	The image intensity plot of day 117, (April 27, 2001). The surf zone appears to both begin and end abruptly, as evidenced from a dramatic transition from regions of intense wave breaking (dark red hues) to areas of little or no wave breaking (blue hues). ....	27
Figure 16.	The environmental data for the first half of the RIPEX/STEEP BEACH experiment discussed in this thesis. The top plot depicts the significant wave height in meters. Wave direction, (degrees from shore normal) from the offshore wave buoy is plotted in the second plot. The third plot illustrates wave period in seconds. The fourth plot depicts the semidiurnal tidal cycle. The bottom plot illustrates the fluctuating surf zone boundaries; blue the upper boundary and red the lower boundary. The black line shows the cross-shore position of the EM tower.....	30
Figure 17.	The environmental data for the second half of the RIPEX/STEEP BEACH experiment discussed in this thesis. The top plot depicts the significant wave height in meters. Wave direction, (degrees from shore normal) from the offshore wave buoy is plotted in the second plot. The third plot illustrates wave period in seconds. The fourth plot depicts the semidiurnal tidal cycle. The bottom plot illustrates the fluctuating surf zone boundaries; blue the upper boundary and red the lower boundary. The black line shows the cross-shore position of the EM tower.....	31
Figure 18.	A plot of EM current sensors in and out of the water column throughout day 108, April 20, 2001. EM sensor number seven (in black) is depicted as being in the water for the duration of the experiment which is incorrect. However by examining the other sensors for example sensor six, one can conclude when sensor seven was most likely in and out of the water.....	33
Figure 19.	The sea surface elevation for day 112.2, displayed for 75 seconds. The blue horizontal line represents the nominal height threshold applied to the sea surface elevation of $1.25 \cdot \text{std}(\eta) + \text{mean}(\eta)$ . A spacing criteria of 6 to 15 seconds was required in order for sea surface elevations to be classified as bores, which are denoted by blue stars at their peaks.....	35
Figure 20.	Horizontal velocity spectra variance ( $\text{m}^2/\text{s}^2$ ) for sensor 6, as compared with its time spent in an out of the water. Low tide is shown to result in an increase in the variance just after day 111.8 this increase ends just before day 112.1.....	38
Figure 21.	Sensor six's horizontal velocity variance ( $\text{m}^2/\text{s}^2$ ), (top plot) as compared with sensor seven's (middle plot) and the sensor immersion fraction for days 110.5 to 114.5. An immersion threshold of .95 was calculated by examining when sensor six's variance increased.....	39

Figure 22.	Horizontal velocity spectra ( $\text{m}^2/\text{s}$ ) of sensor six over the course of a day. Ridges in the spectra correspond to periods of low tide. ....	40
Figure 23.	Horizontal velocity spectra ( $\text{m}^2/\text{s}$ ) of sensor seven over the course of a day. Ridges in the spectra correspond to periods of low tide. These ridges are shorter in breadth in comparison to those found at sensor six. ....	41
Figure 24.	Turbulence dissipation rates for sensors six and seven ( $\text{m}^2/\text{s}^2$ ) (top panel) using the criteria of a .95 sensor immersion; also included are the tide (m), (2nd panel from top), immersion fraction (2nd panel from the bottom) and the significant wave height, (m) (bottom panel). ....	42
Figure 25.	Water depth (H) as compared to the dissipation rate of turbulence ( $\text{m}^2/\text{s}^2$ ) for day 111.2 to 112.2. ....	43
Figure 26.	Borephase thirty minute ensemble averages of cross-shore current velocity (m/s) (top panel), alongshore current velocity (m/s) ( 2 <sup>nd</sup> from top ), sea surface elevation (m) (2 <sup>nd</sup> from bottom) and dissipation rates ( $\text{m}^2/\text{s}^2$ ) (bottom panel) for sensors six and seven for day 110.65 to 110.6917, a period of low wave forcing. ....	44
Figure 27.	Borephase thirty minute ensemble averages of cross-shore current velocity (m/s) (top panel), alongshore current velocity (m/s) ( 2 <sup>nd</sup> from top ), sea surface elevation (m) (2 <sup>nd</sup> from bottom) and dissipation rates ( $\text{m}^2/\text{s}^2$ ) (bottom panel) for sensors six and seven for day 112.2 to 112.2417, a period of high wave forcing. ....	45
Figure 28.	Borephase thirty minute ensemble averages of cross-shore current velocity (m/s) (top panel), alongshore current velocity (m/s) ( 2 <sup>nd</sup> from top ), sea surface elevation (m) (2 <sup>nd</sup> from bottom) and dissipation rates ( $\text{m}^2/\text{s}^2$ ) (bottom panel) for sensors six and seven for day 113.1429 to 113.1846, a period of moderate wave forcing. Note a change in the scaling of the dissipation rates in the bottom panel as compared to the other days in the series. ....	46
Figure 29.	Borephase thirty minute ensemble averages of cross-shore current velocity (m/s) (top panel), alongshore current velocity (m/s) ( 2 <sup>nd</sup> from top ), sea surface elevation (m) (2 <sup>nd</sup> from bottom) and dissipation rates ( $\text{m}^2/\text{s}^2$ ) (bottom panel) for sensors six for day 114.25 to 114.2917, a period of moderate wave forcing. Note a change in scaling of dissipation rates as compared to other plots in the data series. ....	47

THIS PAGE INTENTIONALLY LEFT BLANK

## LIST OF TABLES

Table 1.	The location and spacing of the eight electromagnetic current sensors and capacitance wave wire situated on the vertical tower array used in the RIPEX experiment.....	20
----------	--	----

THIS PAGE INTENTIONALLY LEFT BLANK



## **ACKNOWLEDGMENTS**

I would like to personally thank my friends, family, other IGEP Ensigns and classmates at the Naval Postgraduate School, especially my roommates, Megan and Natalie.

THIS PAGE INTENTIONALLY LEFT BLANK

# **I. INTRODUCTION**

## **A. NAVAL RELEVANCE**

Increasingly the focus of the United States Navy has been the projection of power ashore and maritime dominance of the littoral areas. Achieving these two objectives requires the implementation of amphibious landings, special operations teams, special boat units and other surface support groups. The utilization of manpower, systems and equipment to maximum effectiveness while minimizing risk to achieve mission success requires detailed, accurate and real-time knowledge of the operating environment.

An increasingly exercised and precarious region of the maritime battlefield is the surf zone. Contained within the littorals and nearshore environment, the surf zone is classified as the region between where waves initially break and the shore; this is an area that expands and contracts in response to the tide and wave forcing. Across the surf zone on sandy beaches the bathymetry changes in response to the interaction of sediment transport forced by mean currents, wave motion and breaking waves with the bed. Momentum transfer from breaking waves is primarily responsible for the generation of longshore and cross-shore currents within the surf zone. Turbulence from the shear bottom boundary layer and wave breaking result in the movement of sediment and evolution of sand bars, the formation of rip currents, rip channels and the exposure and concealment of rocks and other sediment outcroppings. The focus of this study is the poorly understood contribution of turbulence from breaking waves in the surf zone that is partially responsible for the dramatic topography, bathymetry, and over time, changes in morphology of a coastline.

Turbulence from breaking waves is of importance as these strong, episodic events can contribute and dominate the suspension of sediment at the ocean bed. The suspended sediment is advected by mean and non-linear wave currents, traveling either down the coastline, shoreward, or seaward, and once settled, creates sand bars within the surf zone. These constantly moving and uncharted sandbars have the ability to ground a SEAL delivery vehicle, a special boat team unit and adversely affect other surface craft in facilitating an amphibious landing, unloading equipment, men or supplies. The building

of a sand bar in one location inevitably results in the depletion of sand in another region. In regions with nearly shore-normal waves, (waves directed perpendicular to the coastline), cross-shore flows often organize into rip channel cells that support strong, dangerous offshore rip currents. Equally debilitating to SEALs, navy divers and other units that rely on the physical abilities of their members are the turbulent velocities under breaking waves, which may be of such large magnitudes that they can result in crippling injuries. It is therefore important to correctly parameterize breaking wave effects in nearshore models.

Improved surf zone models will also increase the Navy's ability to localize mines within the surf zone and nearshore environment. Shallow water bottom mines within the surf zone may shift from their original locations, as a result of direct forcing by currents, waves and scour due to turbulent stresses on the bed. The shifting of sand and sediment has the ability to hide partially or completely mines that were originally exposed to the naked eye.

## **B. AN OVERVIEW OF TURBULENCE**

Turbulence formed by breaking waves is most easily seen by the surface disturbance and bubbles created within the column. Turbulence is dissipative, unlike waves that are dispersive, but not dissipative, (Tennekes and Lumley, 1972). Turbulence from breaking waves is first injected into the water column as large circulating eddies. As time from the breaking event increases these circulating turbulent vortices of kinetic energy slowly transfer energy to smaller scales. The rotating turbulent vortices finally dissipate completely at very small scales, where molecular viscosity begins to dominate the small scale turbulent vortices ability to rotate. Turbulence that reaches the bed structure, can contribute to the bed stresses that serve to suspend sediment within the water column. This can be clearly seen within plunging breakers on a beach face. The turbulent vortices from the breaking waves are of such large magnitudes, and in such shallow water that upon the collapse of the wave, the water can become opaque from the suspended sediment load within the water. Suspended sediment within a water column may then be influenced by both alongshore and cross-shore currents and transported in numerous directions, ultimately influencing the bed-form morphology of beaches.

In order to separate turbulent kinetic energy entrained in the water column by breaking waves from the initial orbital wave kinetic energy, the current velocity profiles of the water within the surf zone region are examined. The profile of the mean flow velocity in a water column over a rough bed results is logarithmic. This logarithmic profile begins at the rough bed and extends upwards towards the surface (Kundu, 1990). Breaking waves inject turbulence into the water column at the sea surface. The turbulence extends downwards into the water column and homogenizes the once logarithmic profile as depicted in Figure 1.

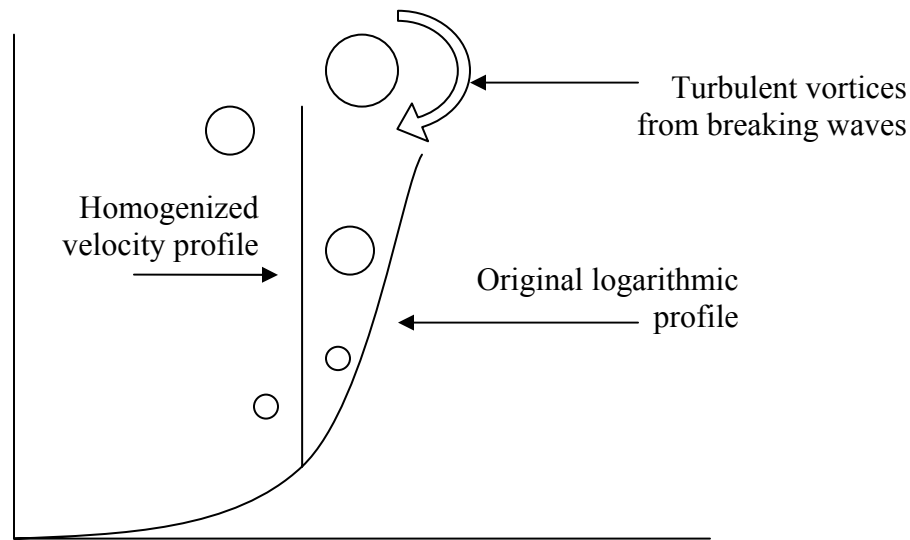


**Figure 1. Turbulent eddies entrained within the water column by breaking waves homogenize the logarithmic current velocity profile to the depth at which the turbulence extends.**

Within the surf zone, the water column may be divided into three regions; the surface wave and wind boundary, the bottom boundary layer and an interior layer. At the bed, a no-slip condition exists, with mean and turbulent velocity components dissipating completely at the bed. However, viscous forces, (and not turbulence) can exist in a thin linear layer above the bed. Within the laminar sub-layer, or viscous sub layer, the average current velocity is linear as seen in Figure 2. The resulting bed stresses from the current above is related to the turbulent friction velocity through Equation 1.

$$u_* = \sqrt{\frac{\tau_o}{\rho}} \quad (1)$$

Within the surf zone, rough bed structures are typically larger than the thickness of the viscous layer yield and result in larger bed shear stresses than smooth beds, and consequently larger bed shear stress coefficients.

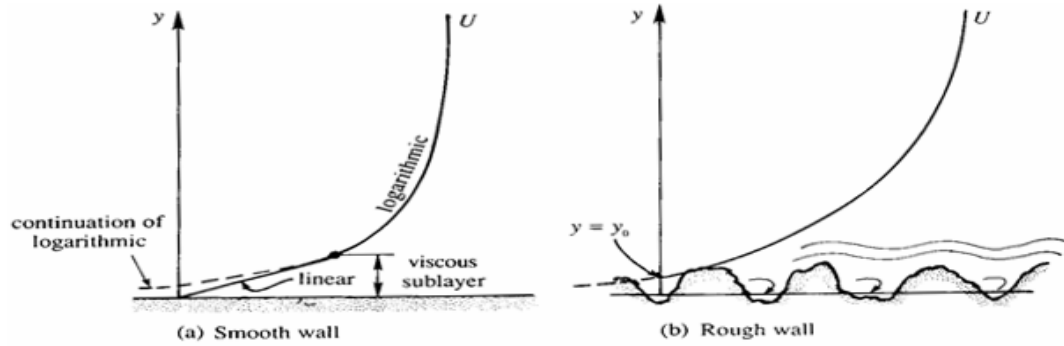


**Figure 2. (From: Kundu, 1990). Logarithmic velocity distributions near smooth and rough surfaces**

The horizontal velocity components used in estimating the bed stress coefficients include both the orbital and turbulent velocity components, (Faria, et al, 1998). Both alongshore currents and sediment transport rates are direct functions of the bed shear stress coefficient,  $C_f$ .

$$C_f = \frac{v_*^2}{(u^2 + v^2)^{1/2} \nu} \quad (2)$$

In a study conducted by Faria et al. (1998) the bed shear stress coefficient was found to be negatively correlated with the percentage of wave breaking.

The interior layer, and majority of the water column, is the region between both boundary layers. Cox and Kobayashi (1996) conducted laboratory experiments on cross-shore current velocities for rough and smooth sloping bed bottoms within a surf zone. Cross-shore velocity profiles were measured at six different locations above the laboratory engineered beds including: the shoaling region seaward of breaking, the break point, the transition region, and the inner surf zone. Their resulting kinematic undertow

models defined the cross-shore current velocity profile as logarithmic. The first analysis specified the volume flux below the wave trough level, and the second (more applicable to field measurements) prescribed a measured undertow for a given elevation within the water column. Each method resulted in the same conclusion that a logarithmic profile best described the mean current velocities for the bottom boundary layer, both in and out of the surf zone, (Cox and Kobayashi, 1996). The logarithmic profile of current velocity in the water column is more readily associated with steady flow in rivers and channels, but may also be applied as a model for ocean surf zone mean current profiles even in the presence of waves.

The DUCK 94 field experiment conducted off the coast of Duck North Carolina at the Army Corps of Engineers Field Research Facility in 1994 provided observations of the alongshore mean current structure in the surf zone. Analysis of the experiment centered on the most robust time periods when winds, waves and currents were the most intense. Results of the field data depicted the vertical alongshore current velocity as having a logarithmic profile, as illustrated by Figure 3, (Faria et al, 1998).

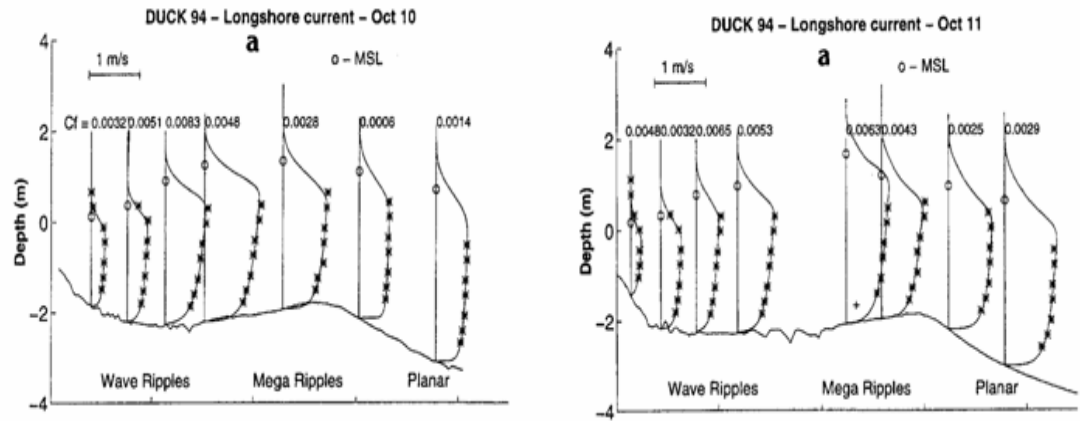


**Figure 3.** (After: Faria et al., 1998). Results of the robust days depicted a logarithmic profile for the mean longshore currents. Depicted are the measured (asterisk) and predicted (line) vertical profiles, superposed on bottom profiles with mean surface sea elevation indicated by open circles and measured  $C_f$  values.

As expected, this logarithmic profile did not extend all the way to the surface, as wave breaking and turbulence homogenized the profile in the upper portions of the water

column. The general equation for the logarithmic profile of both cross-shore and alongshore current velocities as observed by Cox and Kobayashi, (1996) and Faria et al., (1998) is expressed (Kundu, 1990).

$$\frac{U}{u_*} = \frac{1}{\kappa} \ln \frac{y}{y_0} \quad (3)$$

where  $u_*$  is friction velocity,  $\kappa$  the Von Karman constant (0.4),  $y_0$  represents the measure of the roughness height where the mean current velocity intersects 0 (a no slip condition.). Observations across the surf zone were made by moving the tower instrument array back and forth in the cross-shore direction on a mobile sled. The sled was moved offshore each day by the CRAB, (Coastal Research Amphibious Buggy), and then dragged onshore in 50 meter increments approximately hourly throughout the day. Other instruments included in the DUCK Experiment were cross-shore and alongshore pressure and current arrays, in addition to buoys in the deeper waters of the experiment (Figure 4.)

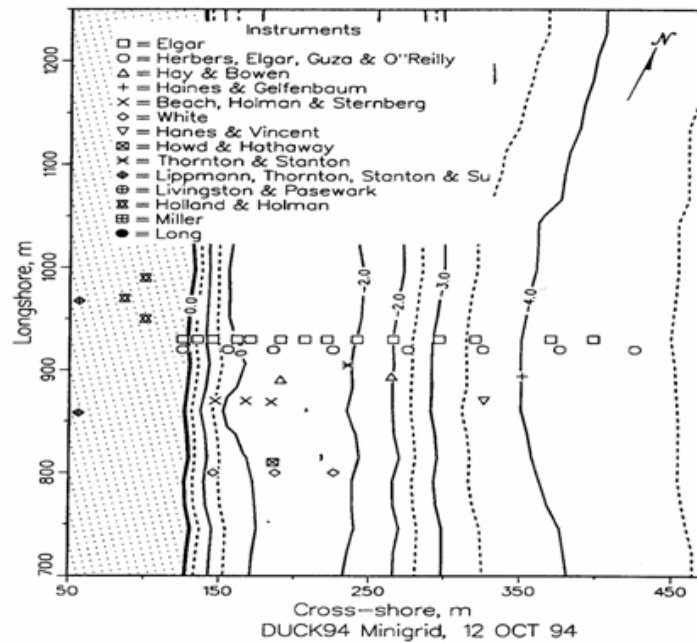


**Figure 4.** (From: Faria et al, 1998). A diagram of the placement of alongshore and cross-shore instrument arrays in the Duck 94 Experiment.



The vertical profile of the alongshore current obtained from the vertical tower of current sensors moved across the surf zone allowed the bed shear stress coefficients and bottom roughness to be estimated. Data collected from the experiment indicated that wave breaking and turbulence within the surf zone decreased the bottom shear stress coefficients. This result was presumed a consequence of the relationship that exists between wave breaking and the undertow velocity, with increases in breaking waves prompting increases in undertow velocity resulting in the overall increase in the average cross-shore velocity (Faria et al., 1998).

Turbulence in the water column is a result of three sources: the thin oscillatory wave boundary layer, the river-like mean current boundary layer above the bed and the strong episodic wave breaking events superimposed on these two other boundary layers. However, measuring turbulence intensity within the surf zone is complicated by intermittence, the strong oscillatory motion of the waves and the highly nonlinear, random nature of breaking waves. Waves break when the fluid at the surface moves at velocities faster than the phase speed of the wave. As a wave approaches the shore, the water depth becomes shallower, the shallower water depth prompts the waves to become progressively steeper, ultimately cresting and breaking (Thornton, 1979).

Energy density spectra of wave velocity components in either frequency or wavenumber space depict the rates at which turbulent kinetic energy is dissipated within the water column. Prior to a wave breaking within the surf zone, the energy and momentum of the wave is transferred up the frequency spectrum. Upon breaking, the energy is transferred back down the velocity spectrum into the outer scales of turbulent motions and into wave harmonics. Wave velocity spectra may be effectively divided into three distinct regions. The first region, with its characteristic large peak, represents the initial orbital wave velocities. Kinetic energy due to turbulence can be large at these low frequencies or small wavenumbers, but is still masked by the larger orbital wave velocity components. This makes separation of the orbital wave energy from the turbulent wave energy difficult. The second region, is known as the inertial sub-range, identified by its consistent slope of  $(-5/3)$ , as seen in Figures 5 and 6. In the inertial sub-range, the kinetic energy of the turbulent eddies cascade down from the initial outer scales of the intensities and turbulence at low wave numbers, to those of high wave numbers. Only the transfer

of energy by inertia forces (vortex stretching) takes place in this range (Kundu, 1990). The inertial subrange is the region of the spectrum which may be exploited to determine the dissipation rate, ( $\varepsilon$ , in units  $\text{m}^2/\text{s}^3$ ) of turbulent kinetic energy under breaking waves. The third region of the spectra is referred to as either the dissipating range, or the viscous range. Within the viscous range, the ability of small turbulent vortices to rotate are slowed as molecular viscosity begins to dominate and dissipate the vortices at these levels.

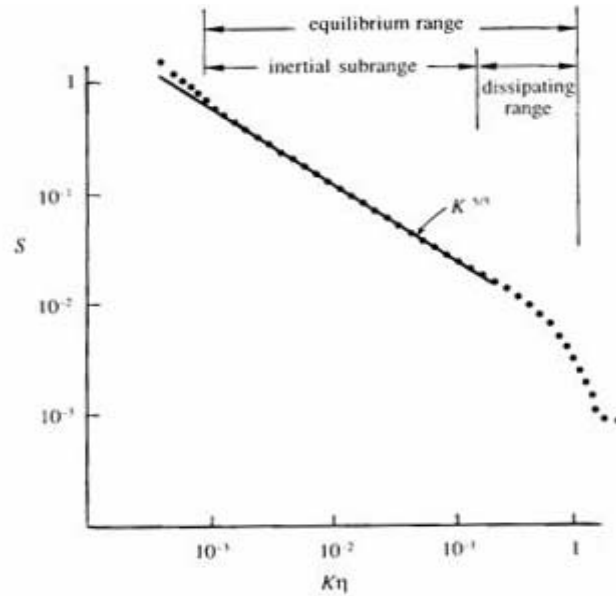


**Figure 5.** (From: Kundu, 1990). Two of the three regions of a wave's energy density spectra are depicted, the inertial subrange with its characteristic  $(-5/3)$  slope and the dissipation range, where molecular viscosity begins to dominate the turbulent eddies ability to rotate.

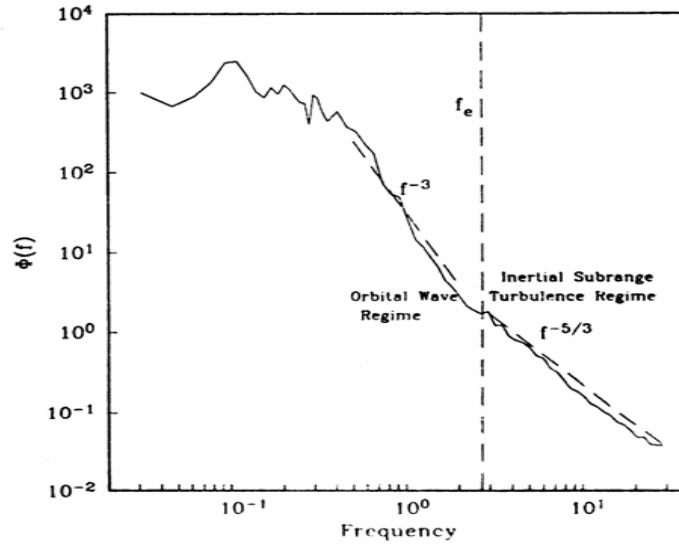


**Figure 6.** (From: George et al., 1994). A frequency spectrum from a hotfilm time series showing the orbital wave ( $f^{-3}$ ) slope and inertial subrange turbulent ( $f^{-5/3}$ ) regimes

A study conducted offshore and just outside the surf zone found turbulence levels to be two to three orders of magnitude less energetic than initial orbital velocities, (Trowbridge and Elgar, 2001). However, because the experiment was not within the bounds of the surf zone where continuous wave breaking is occurring, turbulence intensity measurements should be expected to be much smaller than those within the surf zone.

There are several methods used to calculate the dissipation rate of the turbulent eddies from breaking waves within the surf zone. Two methods used in this thesis adopted from methods by Trowbridge and Elgar (2001) and George et al., (1994) who examined the inertial velocity frequency and wavenumber spectra of the current velocity components to obtain rates of dissipation.

Dissipated energy must be transferred across the energy spectrum from low to high wavenumbers to scales where molecular viscosity dissipates the energy. As little dissipation occurs within the inertial subrange, only small segments of the inertial subrange are required to be resolved in order to calculate the dissipation rate associated with the spectra. At high wavenumbers the velocity field is nearly isotropic; the spectrum does not depend on how much energy is present at large scales where most of the energy is present, but instead only on the parameters that determine the nature of

small scale flow. Consequently, the wavenumber spectrum  $S(K)$ , within the inertial subrange may be represented by Equation 5, where  $A$  is equal to 1.5,  $l$  is a typical length scale of the large eddies,  $\beta$ , the length scale of small eddies, and  $\varepsilon$  is the dissipation rate (Kundu, 1990).

$$S(K) = A\varepsilon^{2/3} K^{-5/3} \quad l^{-1} \ll K \ll \beta^{-1} \quad (5)$$

In order to map time sampled velocity data into spatially sampled data (from which wavenumber spectra can be calculated), Taylor's hypothesis is invoked for steady flows. In Taylor's hypothesis, the turbulent velocity structures are advected past a fixed sensor by the mean current. As the water velocities move past the fixed sensor, the turbulent velocities appear "frozen", allowing an accurate depiction of both the turbulent and mean current velocities. The validity of Taylor's hypothesis and the ability to resolve the turbulent velocity from the mean current velocity depends on the turbulent velocity being much smaller than the mean advective current velocity. Resolving wavenumber spectra in oscillatory flow like the surf zone is challenging as Taylor's hypothesis is violated as the wave velocity goes through a zero value with each half wave cycle. Turbulent velocities under breaking waves near the surface, while masked by the mean current velocities are likely similar in magnitude to the mean current velocity.

Examining the horizontal velocity components, Thornton (1979), attempted to separate the measured wave-induced velocities from the turbulent velocity components within the surf zone. Velocity was separated into its three components, as seen in Equation 6; the mean velocity value  $\bar{u}_i$  for convenience was subtracted out of the signal or assumed to be zero. The wave-induced velocity,  $\tilde{u}_i$ , was assumed to be coherent with the wave surface elevation and any incoherence between the sea surface elevation and the velocity field, is attributed to the turbulence velocity,  $u_i'$ .

$$u_i = \bar{u}_i + \tilde{u}_i + u_i' \quad i=1,2,3 \quad (6)$$

The observations were made at three different beaches; Del Monte, Torrey Pines and Carmel River Beach, each beach exhibiting different types of breaking waves. Although turbulence is more rapidly dissipated in plunging breakers than spilling breakers, the process for generating turbulence within the water column remains the

same. Measurements were made in Thornton's studies outside, at and inside the surf zone of Del Monte Beach. Steeper slopes within the saturation region of the surface elevation spectra illustrated that in deeper water outside the surf zone energy was much more slowly transferred down the spectrum. Plunging waves were shown to have steeper surface and horizontal velocity spectra as compared with spilling breakers as evidenced by Figure 7.

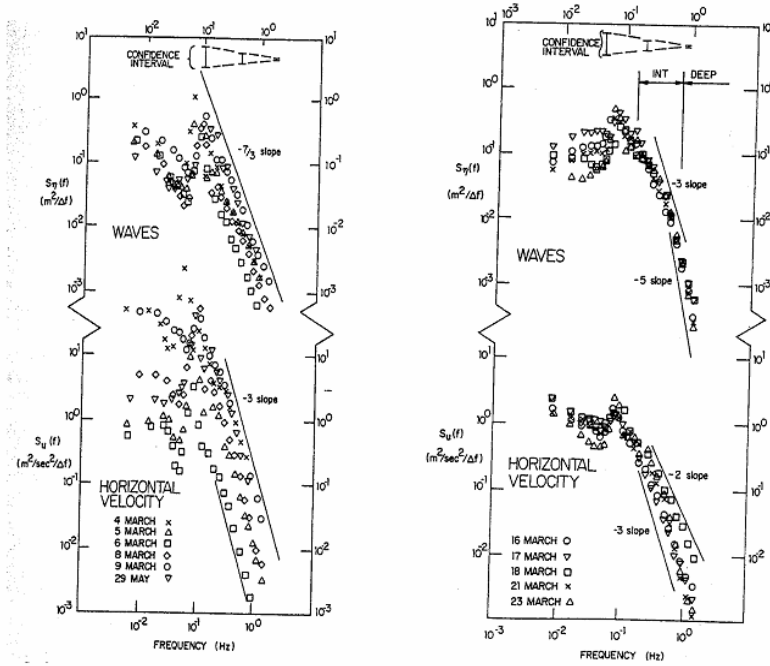


**Figure 7. (From: Thornton, 1979). Horizontal and surface elevation spectra, the left panel for plunging breakers and the right for spilling breakers.**

To separate the horizontal orbital wave velocity from the horizontal turbulent wave velocity, Thornton compared the cross-spectral coherence between the wave-induced horizontal velocity (Equation 8) and the wave surface elevation, (Equation 7) keeping height, depth, wavenumber and frequency as constant parameters. This linear approach of using coherence spectra to separate the horizontal wave-induced velocity from the turbulent velocities, attributed any incoherence in the ratio between wave-induced velocity and the wave surface elevation, Equation 9, due to the turbulence velocity components.

$$\eta(t) = a(f) \cos 2\pi ft \quad (7)$$

$$u(t) = \left( \frac{\cosh k(h-z)}{\sinh kh} \right) a(f) \cos \left( 2\pi ft - \frac{\pi}{2} \right) \quad (8)$$

$$\left( \frac{|u(t)|}{|\eta(t)|} \right) = \left( -i2\pi f \frac{\cosh k(h-z)}{\sinh kh} \right) \quad (9)$$

Using this method of separation to determine the contribution of turbulence to the average kinetic energy, seventy percent was attributed to the waves and thirty percent attributed to turbulence. However, this linear filtration approach in separating turbulence from the wave orbital velocity was shown to have a problem by Herbers and Guza (1993). In Thornton's measurements only velocities in the horizontal direction were measured and as a result, the directionality of the incoming waves reduced the relative coherence between surface elevation and the orbital wave velocity. Thornton's approach had neglected the effect of the directional spreading of incoming waves which reduces the coherence between wave-induced velocities and wave surface elevation. Consequently, the amount of kinetic energy attributed to turbulence in the water column in Thornton's study was overestimated (Herbers and Guza, 1993). To avoid such errors, the RIPEX/STEEP BEACH vertical instrument tower array included one electromagnetic sensor which measured the vertical wave-induced velocities, as vertical velocities do not de-correlate with increased directional spreading.

To estimate turbulence intensity from breaking waves, George et al., (1994) examined the energy density spectra of both horizontal velocity components. Their experiment, conducted over six days in March and April 1992 off the coast of Scripps Beach in La Jolla California, measured data from three vertical hotfilm velocity sensors, two electromagnetic current meters, and a pressure sensor. Using Taylor's hypothesis for short 1 second time periods of the u component velocity were resolved and converted from frequency space to wave number space. A line of best fit of -5/3, the slope of the inertial subrange, was applied to the wavenumber spectrum. Using this line, epsilon was estimated from the spectral level of the inertial subrange. A second method estimated the dissipation rate by integrating the dissipation spectrum measured by high spatial resolution hotfilm sensors over the inertial and viscous sub-ranges. Both adopted

methods resulted in epsilon values within a factor of two of each other. Average dissipation rates were calculated following the method employed by Baker and Gibson (1996). As epsilon is assumed to be a lognormally distributed random variable, an accurate average dissipation rate is not only the calculated mean epsilon, but also the addition of half the variance, known as intermittency. Failure to include the intermittency in calculating the average dissipation rate would result in an underestimation of the mean dissipation rate (Baker and Gibson, 1986). Turbulence intensity was also calculated using Thornton's 1979 proposed method, in which incoherence between sea surface elevation and orbital wave velocities were attributed to turbulence. These biased intensity estimates, along with the various estimated dissipation rates were compared to a hydraulic jump model, and other laboratory data. The calculated field turbulence intensities, despite their bias were shown to agree with intensities predicted from a macroscopic bore dissipation mode, (George et al., 1994).

Trowbridge and Elgar (2001) measured turbulence dissipation rates by adapting a method proposed by Lumley and Terray (1983). Lumley and Terray (1983) showed that a random wave field modifies the characteristic slope of the inertial subrange in a predictable way when there is no dynamic coupling between the waves and turbulence. A field of long crested (uni-directional waves) monochromatic waves were aliased with turbulent energy, the incorporation of drift currents yielded the inertial subrange slope of  $-5/3$ . However, Lumley and Terray's method grossly violated conditions of Taylor's frozen turbulence hypothesis.

Trowbridge and Elgar (2001), studied the balance of stress in the nearshore by examining the balance between near bottom turbulent Reynolds shear stresses and surface stress with wind and radiation stresses (momentum flux) from wave breaking in the water column. Their experiment at Duck North Carolina obtained measurements using several upward looking acoustic Doppler velocimeters placed in a linear array three hundred meters from the shoreline. In measuring Reynolds stresses and shear, they also calculated the turbulence dissipation rate. Results of their study observed near bottom turbulent Reynolds shear stresses were smaller than wind and wave forcing by a factor of two. Kinetic energy dissipation and local shear production was well correlated, and their magnitudes were two orders smaller than the depth averaged rate at which shoaling

waves lost energy to breaking. These results, as stated earlier, can be attributed to the fact that turbulence did not penetrate down to the measurement depth, and that the experiment took place outside the surf zone, (Trowbridge and Elgar, 2001).

Trowbridge and Elgar (2001) examined the dissipation rate and shear production with the wave velocity spectra in frequency space. To accurately represent both the horizontal and vertical velocity spectra  $P_{uu}(\omega)$ ,  $P_{vv}(\omega)$  in frequency space ( $\omega$ ) measured by a fixed sensor in a dominantly oscillatory flow they applied a modifier of  $I\left(\frac{\sigma}{V}, \theta\right)$  (Equations 10-12), with  $V$  the magnitude of the current,  $\sigma^2$ , the variance of the wave-induced horizontal velocity and  $\theta$ , the angle between waves and current. The relations between sigma over velocity and theta is plotted in Figure 8.

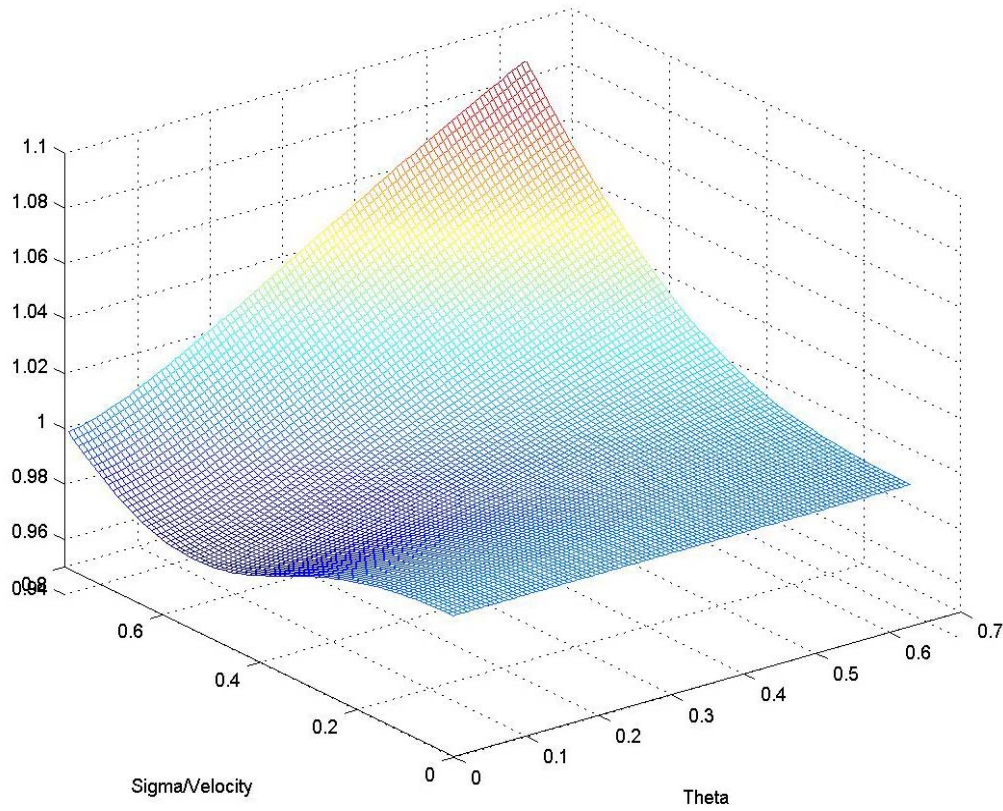


**Figure 8.** The modifier  $I\left(\frac{\sigma}{V}, \theta\right)$ , and the relationship between sigma/velocity and theta.



Solving for the dissipation rate,  $\varepsilon$ , simply requires the summation of both the horizontal velocity component spectra, and the transfer of variables defined in Equation 12 to the other side of the equation. For their experiment,  $V$ ,  $\sigma$  and  $\theta$  were set equal to the mean horizontal velocity. The resulting calculated dissipation rates for the vertical and horizontal velocities were then averaged together to produce a single estimate of dissipation,  $\varepsilon$ .

$$P_{uu}(\omega) + P_{vv}(\omega) = \frac{21}{55} \alpha \varepsilon^{2/3} V^{2/3} \omega^{-5/3} I\left(\frac{\sigma}{V}, \theta\right) + \text{constant noise level} \quad (10)$$

$$P_{ww}(\omega) = \frac{12}{55} \alpha \varepsilon^{2/3} V^{2/3} \omega^{-5/3} I\left(\frac{\sigma}{V}, \theta\right) \quad (11)$$

$$I\left(\frac{\sigma}{V}, \theta\right) = \frac{1}{\sqrt{2\pi}} \left(\frac{\sigma}{V}\right)^{2/3} \int_{-\infty}^{+\infty} \left[ x^2 - 2 \frac{V}{\sigma} \cos(\theta) x + \frac{V^2}{\sigma^2} \right]^{1/3} \exp\left(-\frac{1}{2} x^2\right) dx \quad (12)$$

THIS PAGE INTENTIONALLY LEFT BLANK

## **II. RIPEX/STEEP BEACH EXPERIMENT**

### **A. OVERVIEW**

The RIPEX experiment was part of a larger field study known as RIPEX/STEEP BEACH that had an intensive observation period from on 13 April 2001 and ended 23 May 2001, in Sand City California. The objectives of RIPEX/STEEP BEACH included the comprehensive measurement of a rip current system in the field, and numerical modeling of measurements of wave transformation, breaking wave and current-induced turbulent bottom and surface boundary layers, and sediment flux within the surf zone. Conducting quantitative field measurements of rip currents are considered difficult due to difficulties in installing instruments, the migration rip current channels, or the rip channels themselves being too broad or poorly defined. However, understanding rip current systems are important, as rip currents are not only a large contributing factor to sediment transport, but also shoreline evolution and beach safety. Prior to RIPEX/STEEP BEACH, rip currents had been largely studied on beaches with relatively simple beach morphology with few in situ measurements. The RIPEX/STEEP BEACH experiment expanded on an existing ONR experiment on steep beach dynamics within Monterey Bay and was partially funded by the NSF. The experiment was conducted on a barred beach in Sand City, consisting of a highly reflective slope of 1:20 offshore and 1:5 at the beach face. This beach was selected in particular due to the nearshore processes in this location being largely dependent upon the local bathymetry; the result was a beach that consisted of a strongly perturbed, stationary, nearshore crescentic bar system, with well-defined rip channels. This beach situated off of Monterey Bay is ideal for study, as the sheltering headlands and strong refraction over the Monterey Submarine Canyon typically provide energetic, narrow banded, and near normally incident waves to the beach, which produce well-defined rip current systems. The experiment spanned the month of April covering the spring low tide and neap cycle, permitting the entire surf and swash zone to be measured over the tidal cycles. To gather the field data for the experiment, long term video imagery, bed morphology from a sonar and kinematic GPS personal water craft, cross-shore and alongshore arrays of in situ current and pressure sensors (puv) were used to resolve the mean circulation, wave transformations and

infragravity waves across a shoal rip/channel cell. Over the course of RIPEX/STEEP BEACH, extensive observations of wave characteristics and currents were made including setup and setdown, current velocities, sediment transport and induced turbulence from both the surface and bottom boundary layers. Measurements from the experiment are used to determine differences between steeper beaches, such as that in Sand City, California compared to beaches with more gradual slopes such as Duck, North Carolina, and the site of several previous large-scale nearshore experiments.

## **B. PHYSICAL EXPERIMENT**

A vertical tower located near the intersection of the alongshore/ cross-shore arrays was equipped with an array of electromagnetic current sensors and a capacitance wave staff. Long-term digital camera time-lapse recordings of the experiment site within the surf zone were used to map morphology changes of the surf zone from April 16, 2001 (day 107) to April 30, 2001 (day 120). The dataset consists of multiple surf zone properties. Of highest interest and importance in the dataset are the properties of individual well-defined bores over half hour time intervals and their properties, which include the velocities, sea surface elevation and most important turbulent energy dissipation rate. Other important factors that are examined were the duration electromagnetic current sensors spent both in and out of the water, cross-shore image intensities of the surf zone from the digital cameras, and the environmental data from the experiment including the wave period, significant offshore wave height, wave direction and the tidal cycle.

The vertical tower array of sensors was situated in the surf zone of Sand City at 105.69 meters in the cross-shore direction and 48.45 meters alongshore direction from the experimental coordinate datum, denoted as M +G for the Mast and Goal Post in Figure 9. In addition to the vertical instrument array analyzed in this thesis, the RIPEX/Steep Beach experiment also included other EM current sensors, pressure sensors and buoys in the various depths in both the alongshore and cross-shore directions. The data from the RIPEX /STEEP BEACH experiment used a normal coordinate system, with x+

indicating offshore, and  $y^+$  alongshore towards Monterey. For example, incoming waves to shore were in the negative  $x$  direction, and alongshore currents toward Monterey were positive.

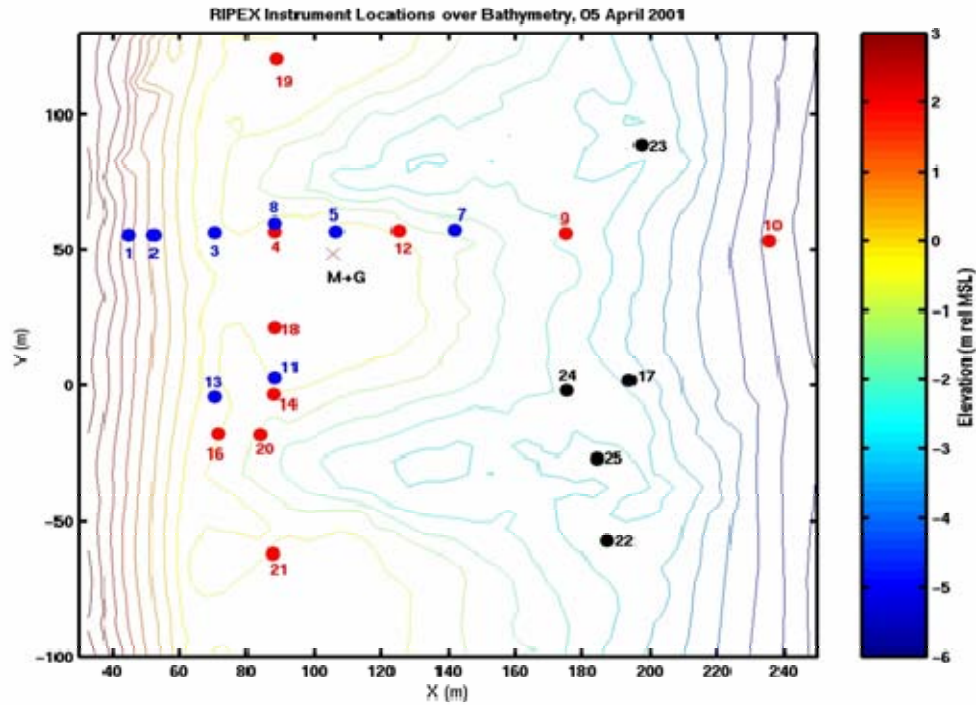


**Figure 9.** (From: Stanton T.P, 2002). The location of the vertical tower array situated within the surf zone and other sensors used in the RIPEX/STEEP BEACH experiment. The vertical tower instrument array is delineated as “Mast and Goal Post” or “M+G”.

## C. INSTRUMENTS

### 1. Electromagnetic Current Meters

The vertical tower array supported eight Marsh McBirney, sensor model 512 electromagnetic, analog circuit, 2 axis current meters. The current sensors had internal 4 Hz cutoff frequency, two-pole low-pass Butterworth linear-phase filters, and were synchronously over-sampled with all other sensors at the boundary layer and bottom boundary layer frame. The EM sensors can measure fluid velocities even in large bubble and sediment concentrations. By using the Faraday Electromagnetic Induction principle, fluid that moves past the sensor in an oscillatory magnetic field velocity orthogonal to the

sensor electrodes creates a micro-voltage across the sensing electrodes. This voltage is directly proportional to the fluid velocity and is resistance independent.

Seven of the eight current meters measured the current velocities in the cross-shore and long-shore directions. The eighth current meter measured the cross-shore and vertical velocity components, vertical spacing for the EM current meters is shown in Table 1. Data from the electromagnetic current meters was synchronously sampled at 48 HZ and 14 bits and sent through the BCDV current profiler to shore computers. When possible, Macrocytis kelp was removed from the tower at each low tide.

Instrument	TOWER INSTRUMENTS			
	Chan#	x loc	y loc	z loc
EM X1	1	105.69	48.45	2.29
EM Y1	2	105.69	48.45	2.29
EM X2	3	105.69	48.45	1.92
EM Y2	4	105.69	48.45	1.92
EM X3	5	105.69	48.45	1.46
EM Y3	6	105.69	48.45	1.46
EM X4	7	105.69	48.45	1.1
EM Y4	8	105.69	48.45	1.1
EM X5	9	105.69	48.45	0.756
EM Y5	10	105.69	48.45	0.756
EM X6	11	105.69	48.45	0.268
EM Y6	12	105.69	48.45	0.268
EM X7	13	105.69	48.45	-0.156
EM Y7	14	105.69	48.45	-0.156
EM X8	15	105.69	48.19	0.87
EM Y8	16	105.69	48.19	0.87
Vref	29	1	1	0.73
Wave Wire	30	105.69	49.73	-0.14

**Table 1. The location and spacing of the eight electromagnetic current sensors and capacitance wave wire situated on the vertical tower array used in the RIPEX experiment.**

## 2. BCDV

The Bistatic Coherent Doppler Velocimeter, or BCDV, located next to the vertical instrument array tower, shown in Figures 10 and 11, measured water velocities in the water column down to the bed, and also served as an analog to digital multiplexer for the real-time data generated by the ten meter tower's thirty-two data channels and capacitance wave wire. The real time data was transmitted via fiber optic cables to a workstation onshore.

### 3. Wave Wire

A capacitance wave wire located on the tower array consisted of a taught stainless steel wave wire of 1/32 inch diameter that extended from 0.05 meters to 3.0 meters above the bed. When immersed in water the capacitance wave staff generated a voltage proportional to its immersed length that was digitized by the BCDV creating a time series of the sea surface elevation,  $\eta$ , in addition to the height of the mean water level. The wave wire was located 0.3 meters on opposite side of the tower from the electromagnetic current meters to minimize noise that could impact the current meters as seen in Figure 11. During particularly strong wave and wind days, *Macrocystis* kelp continued to be a problem and was removed as frequently as possible. The cross-shore location of the wave wire in comparison to the EM current meters produced a small time delay between the two sensors which had to be resolved. This time delay, however small is significant, as the sea surface height may have changed between the two sensors for wave crest elements not alongshore aligned, resulting in not always knowing when the EM sensors are immersed.



**Figure 10.** Close up snap shot of the vertical tower array of current sensors deployed in the field during the RIPEX/STEEP BEACH experiment. On the left, *Macrocystis* kelp is visible hanging from two of the EM sensors. On the right, the vertical tower array and BCDV situated in the surf zone during the experiment as large waves break in the background.

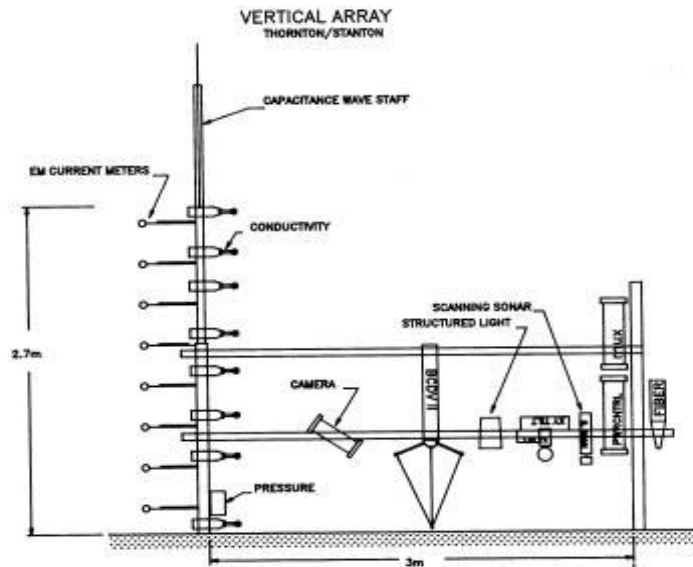


**Figure 11. (From: Stanton T.P and E. B. Thornton., 2002,a,b). A diagram of the vertical tower array of electromagnetic current and conductivity sensors and capacitance wave staff. Also depicted is the BCDV.**

#### **4. Cameras**

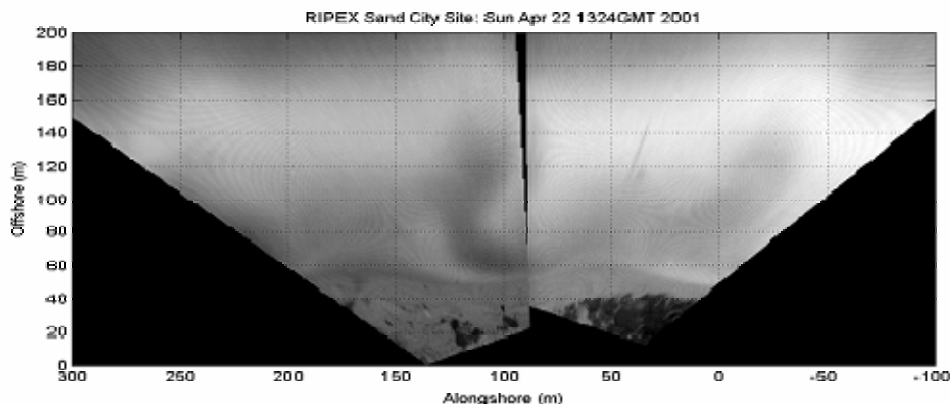
Two ELTEC digital cameras, one facing northward and the other southward used 640x480 CMOS resolution sensors to provide images of wave breaking activity spanning the instrument array. Each camera contained a built-in digitizer and Power PC processor with a web server and Ethernet connectivity. Wipers automatically controlled by the Power Pc were designed to remove salt aerosols from the lens every four hours. The camera tower was 18.7 meters above sea level on a 10 meter tower with its base 8.2 meters above the mean water line, located within the Monterey Regional Water Pollution Control Agency's Wastewater Treatment Plant. Both cameras recorded an ensemble image every twenty minutes of mean, standard deviation, maximum and minimum values of each pixel in the image along with a single snapshot image. Each frame was sampled at 2 Hz automatically, and an internal program automatically adjusted the gain every twenty minutes ensuring that even the brightest pixels were below the camera's saturation limit. The collected data were transmitted by the Ethernet connection to a logging workstation at the Naval Postgraduate School. A snapshot image is shown in Figure 12. Each timex image was transformed into a rectified image, providing a plan view of the



image intensity across the surf zone environment. The rectified timex images (eg. Figure 13) were used to determine the position of the instrument tower within the surf zone. The position of the shoal can be seen as the whiter area along the +80 meter long-shore line; with the darker (lower wave breaking) rip channels on either side.



**Figure 12.** A raw snapshot image taken from the southern ELTEC camera April 22, 2001. The vertical tower array and BCDV are visible within the surf zone. Areas of intense wave breaking within the surf zone are indicated by the regions of brighter (whiter) pixel intensity



**Figure 13.** A rectified image of the surf zone taken April 22, 2001. Dark shading indicate the location of rip currents within the surf zone where fewer waves break in the deeper rip channel. The vertical instrument tower array is visible as the slightly skewed shaded line in the right panel.

## **5. Offshore Wave Buoys**

Two buoys recorded wave direction, significant wave heights and wave periods in Monterey Bay. The first buoy was a National Oceanographic and Atmospheric Association National Buoy Center Buoy (NDBC) #46042 located 40k offshore, the second used exclusively for this experiment was a Datawell Directional Wave Rider buoy (DWR) positioned in waters 18 meters in depth offshore. This second buoy was used to determine offshore wave heights for this study. Wave directions were then transformed for the experiment to fit a shore normal coordinate system. To achieve a shore normal reference, 295 degrees were subtracted from the original data.

## **6. Tidal Data**

Tidal data were provided by the CO-OPS of NOAA/NOS, by referring to station number 9413450, Monterey, Monterey Harbor, in the NOAA National Water Level Observation Network (NWLON).

### **III. RESULTS**

#### **A. IMAGE INTENSITY**

The first step in analyzing the dissipation rate of turbulent kinetic eddies in the surf zone was defining of the surf zone boundaries. Pixel intensities from the digitally rectified images of the northern ELTEC camera were used to both generate the image intensity plots and determine the inner and outer bounds of the surf zone along a cross-shore pixel line intersecting the tower. Each individual pixel in the cross-shore transect of the tower array was evaluated and plotted on a graph of image intensity. From this graph of individual pixel intensities, which extended along the line-of-sight of the tower instrument array, a color scaled graph of image intensity over the course of a day was generated (Figure 14).

The northern ELTEC camera was used exclusively in this experiment to provide the raw images from which both the rectified images and image intensity plots were generated. The northern camera was situated at such an angle that eliminated sun glint from appearing in any raw images and subsequent generated images, and imaged the tower location. Image intensity plots show the surf zone's region of wave breaking and the surf zone's apparent shifts both in breadth and location in response to tide and wave changes over each day's daylight hours. Higher pixel levels are associated with foam and bubbles produced by wave breaking. As illustrated in image intensity plot of Figure 14, areas with red hues were regions of intense wave breaking, and light yellows and greens depicted areas of little wave breaking activity. The areas of particularly intense wave breaking routinely corresponded to the day's low tides. Waves shoaled and broke sooner during the periods of low tide, resulting in larger surf zone widths at low tide.

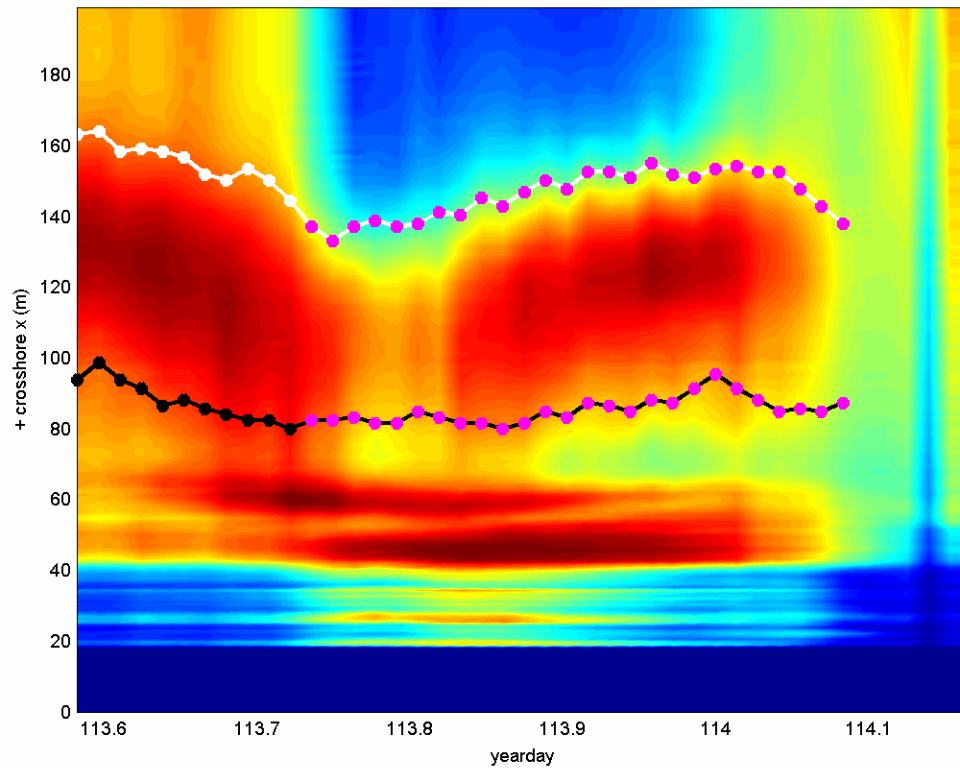


**Figure 14. Image intensity plot of day 113 (April 23, 2001). Both the computer algorithm for the lower bounds (black dots) and the upper bounds (white dots) are visible. Manual manipulations of the surf zone boundaries are indicated by the magenta boundary dots.**

The cross-shore image intensity time series plots also illustrated that regions of intense wave breaking were not limited to the surf zone. Inshore of the surf zone, identified by the connected black dotted lines on Figure 14, a thin region of intense wave breaking is present as a result of run up on the beach face. The raw video timex images and all other measured products were only collected for daylight hours for each day, as there was insufficient light at night to resolve pixel intensity differences. Consequently, each day of the data set extended from 6 am Pacific Time to 8 pm Pacific Time. These time frames were then translated into the Greenwich Mean Time time-base in the experiment, resulting a number system for image intensity in which days began and ended on the their halves. (ie, day 107's image intensity plot began at 107.5 and ended at 108.5.)

For much of the experiment, the image intensity time series represented well the regions of intense breaking waves although days 110 and 117 to 120 (April 20<sup>th</sup> and April 27<sup>th</sup> through April 30<sup>th</sup>) did not produce reliable image intensity figures, as illustrated in Figure 15.

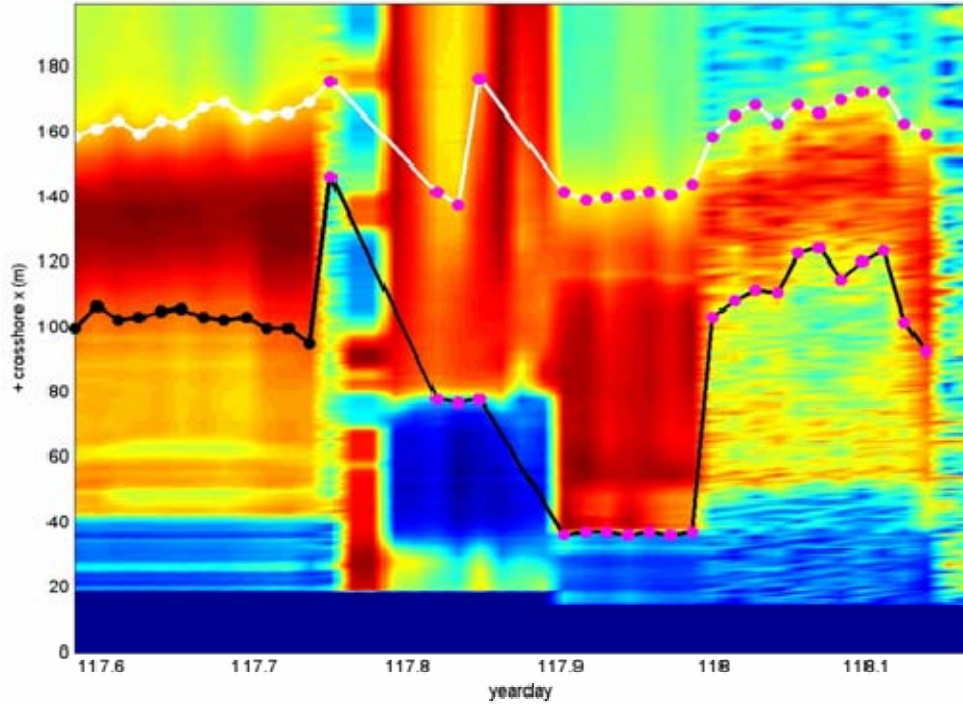


**Figure 15.** The image intensity plot of day 117, (April 27, 2001). The surf zone appears to both begin and end abruptly, as evidenced from a dramatic transition from regions of intense wave breaking (dark red hues) to areas of little or no wave breaking (blue hues).

These inaccurate images intensity plots were caused by the northern ELTEC camera being offset from its original position, as evidenced by the corresponding snapshot and resulting timex images. Snapshot images revealed a camera angle which had inadvertently cut off parts of the beachfront and surf zone used to generate both the rectified images and image intensity plots. Figure 15 may have been the result of a bird perching on the camera.

To create the defined boundaries for the beginning and end of the surf zone, a computer algorithm was applied to the individual profiles of cross-shore image intensity. The beach face region of the cross-shore profile of intensity was omitted in order to

prevent waves breaking on the beach face from influencing the bounds of the surf zone. The lower bounds of the surf zone, illustrated by the connection of black dots, and the upper bounds, illustrated by the connection of white dots, as seen in Figure 14, were selected by use of a computer algorithm that allowed manual override of the surf zone values during difficult lighting conditions. The computer algorithm required that the lower bounds of the surf zone be thirty percent greater than the local minimum rectified image intensity value and the upper bounds seventy percent less than the determined maximum value of image intensity, or thirty percent greater than the end of the pixel resolution, (see Figure 14, a typical cross-shore intensity profile). These inaccuracies were most frequently due to incorrect assignment of local maximum and minimum image intensity values by the computer. Segments of the surf zone boundaries where manual manipulation of the data was used were magenta in color as opposed to the normal surf zone boundary colors of black and white, as seen in Figures 14 and 15. However, in some instances due to the nature of the intensity data, or poor maximum and minimum values, it was not feasible to determine the bounds of the surf zone. In these situations surf zone boundary markers were not plotted at all. These areas were visible by the unequal spacing between surf zone boundary points.

The thirty percent threshold used by the computer algorithm consistently yielded an outer bound of the surf zone that extended farther in the positive x direction than the underlying image intensity figure implied. Likewise, the thirty percent threshold for the computer algorithm generated an inner surf zone boundary that began farther out in the positive x direction than the image intensity plot of the surf zone indicated. However, using these boundaries the vertical tower array was shown to remain in the surf zone for a large portion of the experiment. However, during days 111, and 118 -120, the tower instrument array was outside the surf zone.

## **B. ENVIRONMENTAL DATA**

### **1. Wave Direction**

Wave direction was referenced from shore normal, with a positive direction offshore. Wave direction only fluctuated slightly from shore normal, varying -10 to 10 degrees over the entire course of the experiment, (Figures 16 and 17) due to mainly the

refractive effects of Monterey Bay's submarine canyons that aligned the waves' offshore original northern or southern directions to almost shore normal. The first week of the experiment experienced an increase in significant wave height over day 111 that extended into day 112. The consistent increase in significant wave height of over two meters, recorded at the offshore buoy, most likely resulted from the remains of a distant Pacific Ocean storm. During the second half of the experiment, several short, though less dramatic increases in significant wave height occurred with long period swell beginning on day 119, (Figure 17). At this time wave direction shifted from a southern direction (approximately  $-4$  degrees from shore normal) to a northern direction (approximately  $7$  degrees from shore normal).

## **2. Significant Wave Height**

Significant wave heights ranged from 0.3 meters to 1.9 meters during the experiment. Prior to the large increase in wave height occurring over day 111, the significant wave height had averaged approximately 0.8 meters. Following the large rise in wave height, the average height remained at approximately 1.3 meters, and increased in height of over half a meter. Increased significant wave heights resulted in the shift of the surf zone location in the cross-shore seawards, as illustrated in Figures 16 and 17. For days 111, 112, 119 and 120 the surf zones were all 50 meters farther seaward, extending to almost 200 meters offshore, in comparison to days 109 and 111, on the surf zone only extended to approximately 150 meters in the cross-shore. During days 109 and 110, significant wave heights were at their lowest, 0.3 meters.

## **3. Wave Period**

Wave period was determined by the peak frequency of the wave spectrum. The period varied considerably during the experiment, ranging from 4 to 14 seconds. The dispersive nature of swell waves was often observed with long period swell slowly transitioning to shorter period waves (107-111, 112-114, 119-121). The wave period had a large influence on the intensity of wave breaking within the surf zone, in particular days 111-116. Wave forcing and tides differed for days 111-113 and 114-116. The tidal cycle for the first three days was largely symmetrical, while the semidiurnal tidal cycles for the second three days were asymmetric during spring-tide conditions. Waves were generally shore normal and the significant wave height was over a meter, as was the overall wave

height and direction average for the entire RIPEX/STEEP BEACH experiment. However, during these days of moderate wave forcing the wave period decreased from ten seconds to seven seconds over the first three days, and increased slowly from seven seconds to eleven seconds over the second time interval, (Figures 16 and 17). During day 111 and days 118 and 119, the wave period underwent large fluctuations possibly caused by mixed swell systems. The competing wind and swell sea periods also resulted in surf zone boundaries for these particular days that were more inconsistent and difficult to resolve.

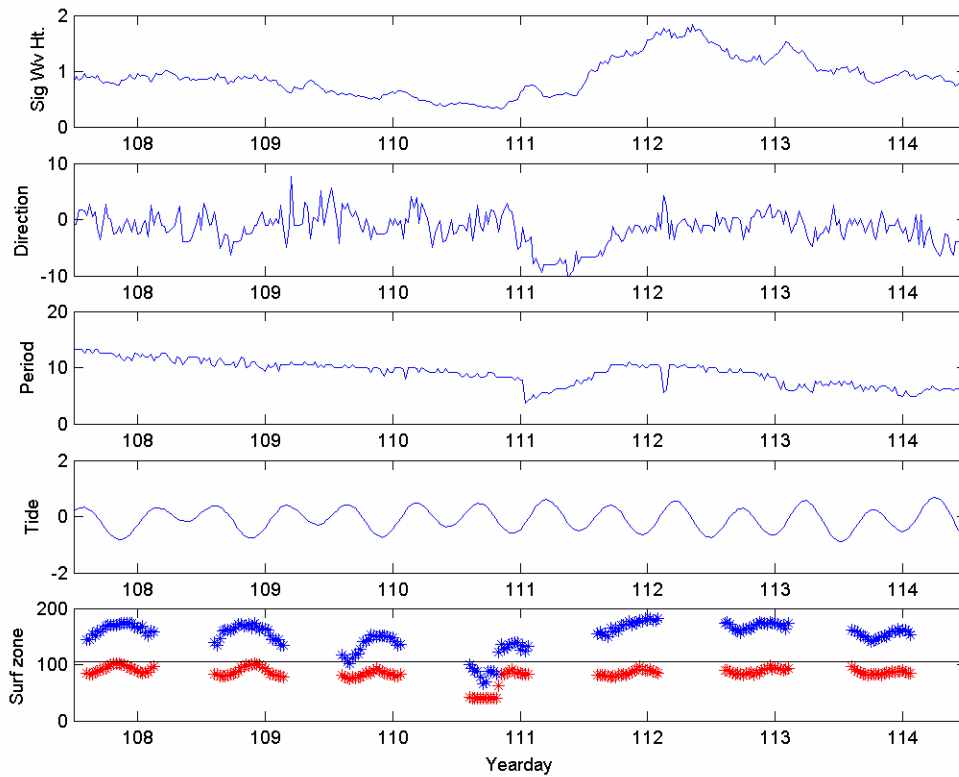


**Figure 16.** The environmental data for the first half of the RIPEX/STEEP BEACH experiment discussed in this thesis. The top plot depicts the significant wave height in meters. Wave direction, (degrees from shore normal) from the offshore wave buoy is plotted in the second plot. The third plot illustrates wave period in seconds. The fourth plot depicts the semidiurnal tidal cycle. The bottom plot illustrates the fluctuating surf zone boundaries; blue the upper boundary and red the lower boundary. The black line shows the cross-shore position of the EM tower.



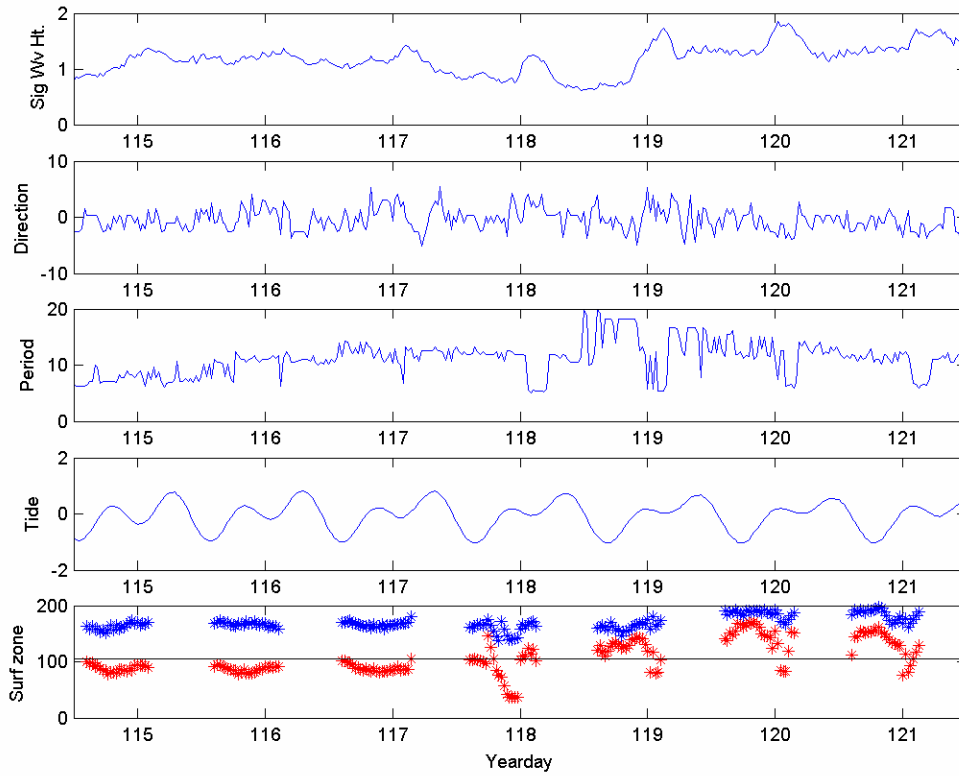


**Figure 17.** The environmental data for the second half of the RIPEX/STEEP BEACH experiment discussed in this thesis. The top plot depicts the significant wave height in meters. Wave direction, (degrees from shore normal) from the offshore wave buoy is plotted in the second plot. The third plot illustrates wave period in seconds. The fourth plot depicts the semidiurnal tidal cycle. The bottom plot illustrates the fluctuating surf zone boundaries; blue the upper boundary and red the lower boundary. The black line shows the cross-shore position of the EM tower.

#### 4. Tidal Cycle

The semidiurnal tidal cycle was the most significant factor in influencing the surf zone location, wave breaking intensity, and breadth, and dictated when the sensors were both in and out of the water. The first week's tides, days 107 to 114, were fairly symmetric with each low and high tide heights similar to each other, in contrast to the second week's spring-tide semidiurnal tides. Variations between the high and low tides occurred during the experiment with the first low tide becoming lower in height than the second, and the same true for the heights of the high tides, illustrated in Figure 16. Whether the current sensors were in or out of the water rested was determined by the tidal

elevation, (Figure 18). EM current sensor number seven, the lowest on the instrument tower remained underwater for most of the experiment. However, graphs of the sensor seven are not accurate, as they depict the sensor as remaining in the water for the duration of the experiment. This is a result of the capacitance wave wire failing to extend low enough in the water column to measure the time that that sensor seven was out of the water. Consequently sensor six's height is used to very conservatively determine the time sensor seven was immersed. The time current sensors six and higher were out of the water all corresponded to periods of low tide. During week two, when the second low tide became less pronounced, each of the current sensors spent increased periods of time underwater. For example, at day 117, differences between both high tides and the second low tide were less than a quarter meter, and sensor six was almost completely submerged for more than fifteen hours. This time interval was substantially longer in comparison to day 113, when both high and low tides were well defined, and sensor six was submerged during each high tide for three hours and thirty six minutes and four hours and forty eight minutes, respectively.

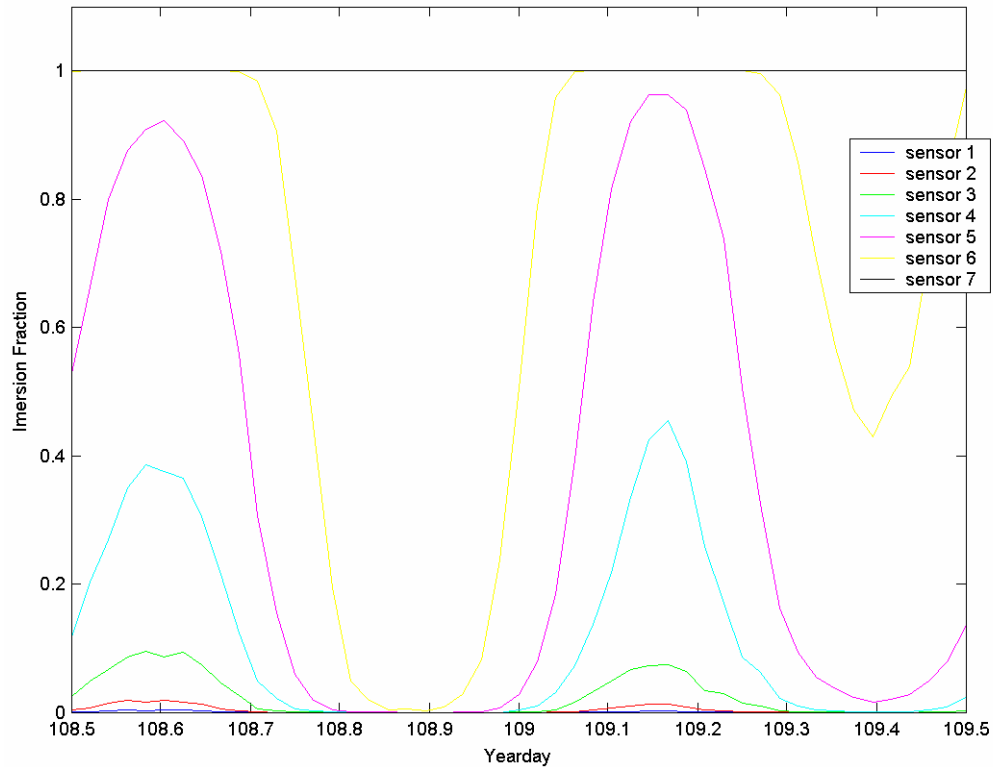


**Figure 18.** A plot of EM current sensors in and out of the water column throughout day 108, April 20, 2001. EM sensor number seven (in black) is depicted as being in the water for the duration of the experiment which is incorrect. However by examining the other sensors for example sensor six, one can conclude when sensor seven was most likely in and out of the water.

The tidal cycle also influenced the overall width of the surf zone. As expected, with wave breaking significantly dependent on the local water depth,  $H$ , during high tides the surf zone shifted seaward, and at low tides the surf zone shifted towards the beach. Increases in surf zone width began just prior to low tide, the time interval ranging anywhere from forty five minutes to as much as two and a half hours before low tide. The fluctuating movement of the surf zone was apparent for most of the days, specifically days 107-109, 112-114, 118-120. The remaining days the surf zone failed to move in either direction in the cross-shore. Similarly, the intensity of wave-breaking was largely dependent on the tidal cycle. Low tides prompted waves to break sooner and increased the intensity of the wave breaking and resulting image intensity from bubble and foam production.

### C. BORE IDENTIFICATION

An analysis of turbulence levels near the bed required identification of individual bores. Thirty-minute records of surface elevation data were analyzed. A bore peak was detected when the sea surface elevation  $\bar{\eta}$  exceeded the mean water depth plus a threshold of the standard deviation of the sea surface,  $\sigma_{\eta}$  (for the thirty-minute time span) multiplied by value of 1.25.:

$$\eta_{threshold} = \bar{\eta} + \sigma_{\eta} * 1.25 \quad (13)$$

The constant 1.25 used in calculating the threshold was determined by trial and error by analyzing many cases with high and low wave forcing. This detection scheme allows detecting bores over both high and low tide intervals in a day. The vertical threshold did not remove all extraneous peaks in the sea surface elevation. These extraneous peaks were often associated with the reflected waves from the shore. To preclude these extraneous peaks from being considered, bores required a temporal threshold as well.

As the average wave period for analyzed data was ten seconds, a temporal bore period ranging from 6 seconds to 15 seconds was required between rises in the sea surface elevation to be classified as a discrete bore. Consequently bores were resolved both temporally and with elevation, as illustrated in Figure 19.

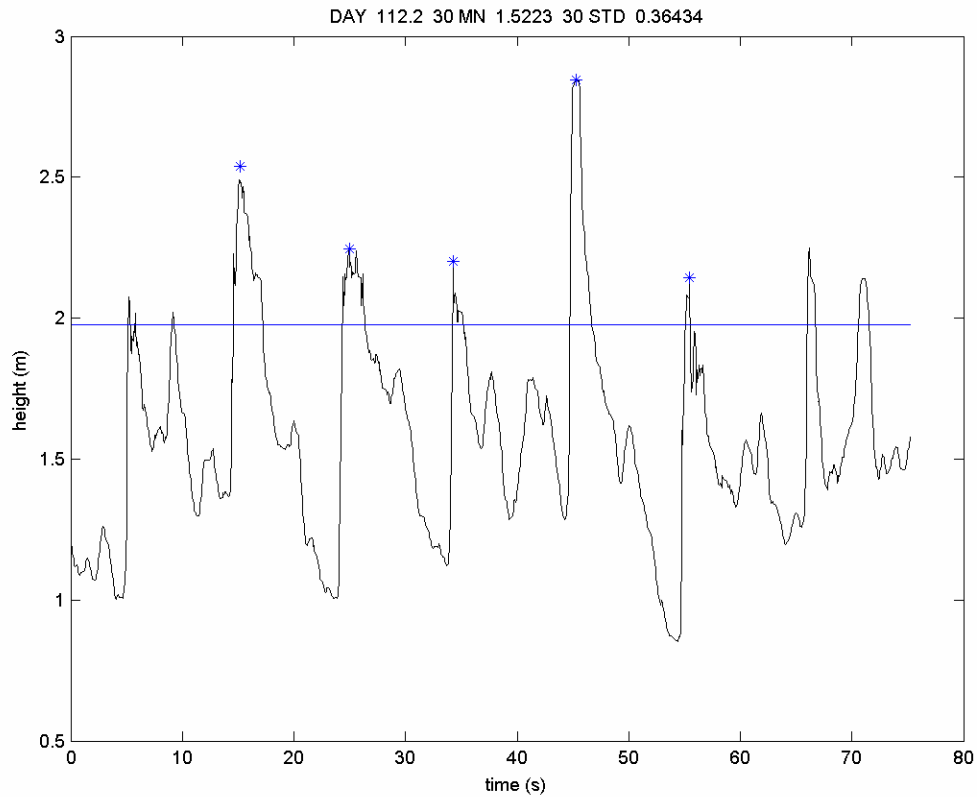


**Figure 19.** The sea surface elevation for day 112.2, displayed for 75 seconds. The blue horizontal line represents the nominal height threshold applied to the sea surface elevation of  $1.25 \cdot \text{std}(\eta) + \text{mean}(\eta)$ . A spacing criteria of 6 to 15 seconds was required in order for sea surface elevations to be classified as bores, which are denoted by blue stars at their peaks.

The dissipation rate and alongshore and cross-shore current velocities were calculated across the phase cycle of each bore for each thirty minute interval. Each bore was divided into thirty equally spaced segments for examining the alongshore and cross-shore velocities, and into ten segments for calculating the dissipation rate underneath each bore. Taylor's frozen turbulence hypothesis was applied to the resulting small segments of the instantaneous current velocity for each resolved bore segments. The ability to resolve very small segments of the instantaneous velocity was necessary due to the strong oscillatory flow and low mean currents to be able to calculate the inertial subrange. The method used for calculating the dissipation rate is similar to the one employed by George et al.,1994. The dissipation rate is calculated by using frequency

spectra translated into wavenumber space by multiplying by the mean current (Equation 14), where the wavenumber spectral form is

$$\Phi(k) = u\Phi(f) \quad (14)$$

$$\Phi(k) = \alpha \varepsilon^{2/3} k^{-5/3} \quad (15)$$

so that

$$\varepsilon = \left( \frac{\overline{\Phi(k)k^{5/3}}}{\alpha} \right)^{3/2} \quad (16)$$

within the inertial subrange. The variable  $\alpha$  is the Kolmogorov constant, equal to 1.5, Trowbridge and Elgar (2001). Intermittency was included in calculating the average dissipation rate for the bore resolution method, to ensure accurate dissipation rates due to the lognormal distribution of dissipation, where

$$\langle \varepsilon \rangle = \bar{\varepsilon} + (\sigma_{\ln \varepsilon}^2 / 2) \quad (17)$$

The second method used to determine the dissipation rate mirrored that used by Trowbridge and Elgar (2001), where continuous spectra were calculated across thirty minute intervals using equally spaced data segments of twenty seconds. Dissipation rates are calculated using energy density spectra frequency space with Equations 10 and 11, including the modifier function  $I\left(\frac{\sigma}{V}, \theta\right)$ . The number of points sampled in the spectra were 128 to maximize degrees of freedom in the inertial subrange.

## IV. DISCUSSION

Data for days 110.5 to 114.5 are analyzed using both the Trowbridge dissipation method and the bore dissipation method. This data was selected because of the steady increase in significant wave height that begins at day 111 and continues into day 112. Low, moderate and high forcing days are all examined during this time period as following day 113 the significant wave height was shown to level off and become relatively stable. The increase in significant wave height that occurred over day 111 and 112 was most likely a result of a large storm that was generated in the North Pacific Ocean. As the wave field entered Monterey Bay the wave direction shifted from its previous direction of relative shore normal (zero degrees) to a more southerly flow of negative ten degrees. This shift to a southerly direction of negative ten degrees was the most dramatic shift in wave direction throughout the entire data series.

The surf zone's breadth shifted seaward with low tide and shoreward with high tide as a result of waves breaking sooner at shallower ocean depths for a given offshore wave height. However, during the rise in significant wave height of over a meter, both surf zone boundaries were shifted even more seaward, with the inner boundary of the surf zone beginning at just under 100 meters in the cross-shore direction and the outer boundary of the surf zone ending just shy of 200 meters in the cross-shore. This contrasts with the time interval that just preceded the rise in wave height. Prior to the large rise in significant wave height that occurred at the end of day 111, significant wave height values measured less than a third of a meter resulting in a narrow surf zone during this time interval. The inner bounds of the surf zone began less than 50 meters from shore and the outer bounds of the surf zone at approximately 80 meters from shore, with the tower array outside the bounds of the surf zone for the first half of the day (Figure 16).

During the beginning of the rise in significant wave height and increasing direction away from shore normal, the wave period also initially decreased from ten seconds to six seconds. As the significant wave height increased though, the wave period slowly returned to ten seconds. Image intensity plots from the cameras recorded wave breaking to be more intense than on previous days. As the wave height remained much

larger than that of the beginning of the data set on days 107 to 111, these days also had more robust wave breaking signatures in the timex video images.

The periods of time when data were unreliable may not only be characterized by low tide intervals, but by also large jumps in the values of the horizontal current velocity variance (calculated by integrating the velocity spectrum) of sensor six, as the sensors entered and left the water injecting strong harmonic signals into the velocity timeseries, (Figure 20). From these linear plots of horizontal velocity variance for sensor six, an immersion threshold of .95 was determined to be required to produced robust values for the dissipation rate and prevent jumps or breakpoints within the horizontal velocity spectra as seen in Figure 21. Constructing the immersion threshold using sensor six's variance also resulted in conservative immersion threshold for dissipation estimates.

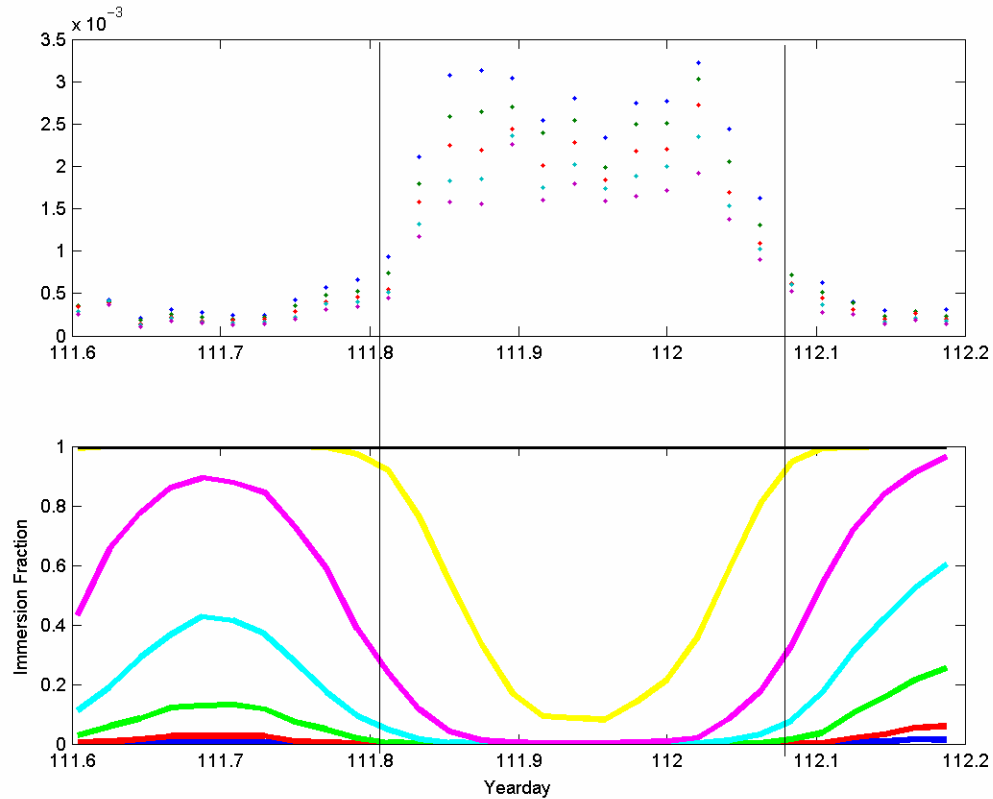


**Figure 20. Horizontal velocity spectra variance ( $\text{m}^2/\text{s}^2$ ) for sensor 6, as compared with its time spent in an out of the water. Low tide is shown to result in an increase in the variance just after day 111.8 this increase ends just before day 112.1.**



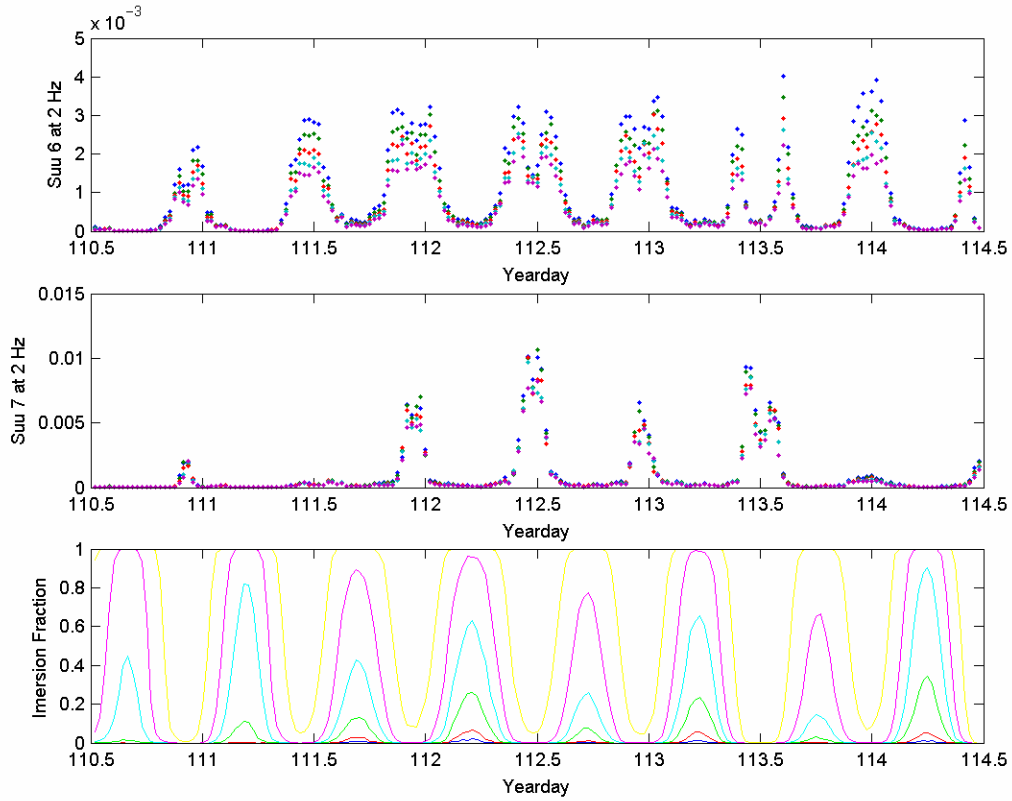


**Figure 21.** Sensor six's horizontal velocity variance ( $\text{m}^2/\text{s}^2$ ), (top plot) as compared with sensor seven's (middle plot) and the sensor immersion fraction for days 110.5 to 114.5. An immersion threshold of .95 was calculated by examining when sensor six's variance increased.

Horizontal velocity energy density spectra as a function of time are shown on Figures 22 and 23. Large ridges in the spectral timeseries at frequency correspond to low tidal periods when the sensors were out of the water. The large ridges are formed in response to the sensors repeatedly being in and out of the water, introducing artifacts into the spectra set. The ridges for sensor seven's three-dimensional spectra are smaller in breadth in comparison to the ridges of sensor six's spectra. This result reiterates the point that during periods of low tide, sensor six was out of the water for longer periods than sensor seven. From the velocity spectra timeseries the initial orbital wave energy range is visible at the very low frequencies in log space. The inertial subrange is seen to begin at about 1 Hz ( $0 \log_{10}\text{frequency}$ ) and end just short of 4 Hz, or 0.5 in the log frequency axis.

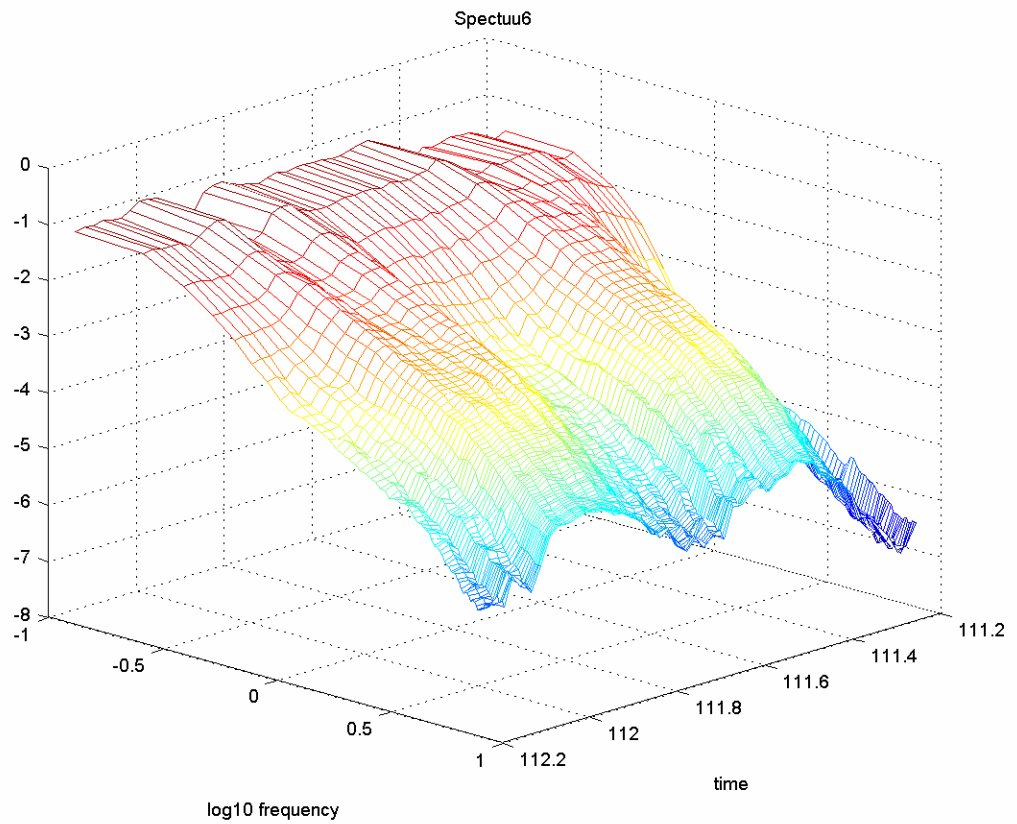


**Figure 22. Horizontal velocity spectra ( $\text{m}^2/\text{s}$ ) of sensor six over the course of a day. Ridges in the spectra correspond to periods of low tide.**

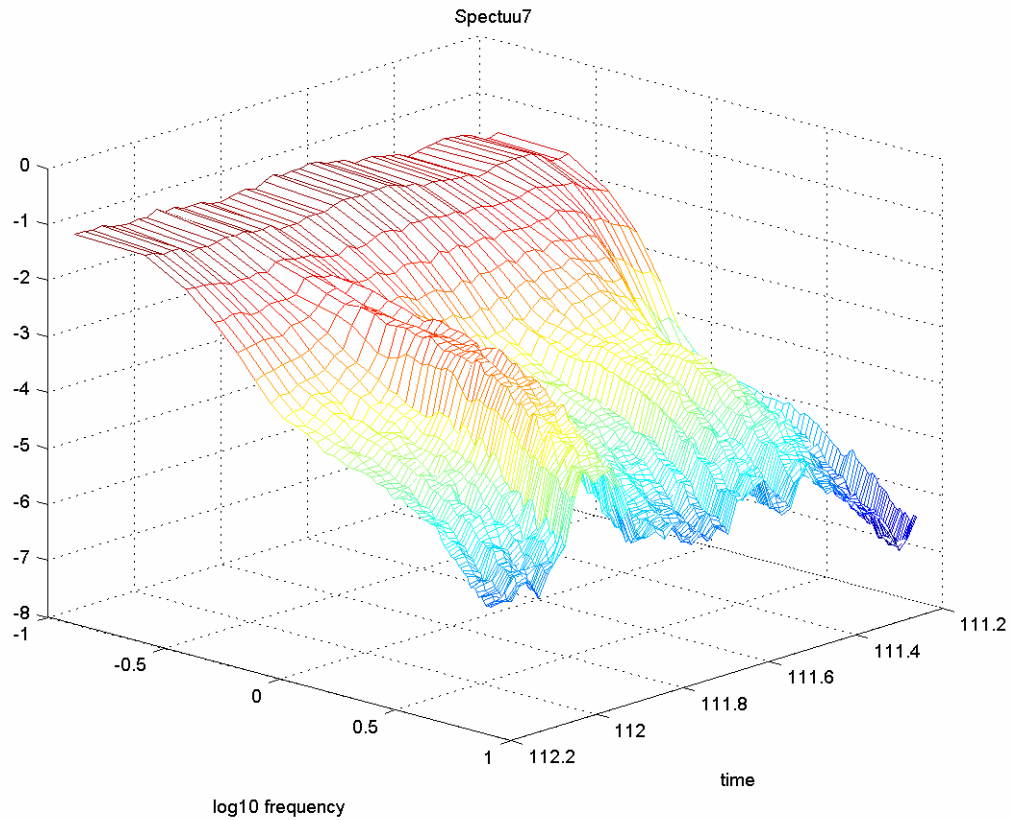


**Figure 23. Horizontal velocity spectra ( $\text{m}^2/\text{s}$ ) of sensor seven over the course of a day. Ridges in the spectra correspond to periods of low tide. These ridges are shorter in breadth in comparison to those found at sensor six.**

Dissipation rates at sensor six and seven were shown to be low during low wave forcing starting on day 110.5 and increased as wave forcing grew (Figure 24). The turbulence dissipation rate reached its highest value during the highest peak in significant wave height that coincided with high tide. Following the rise in significant wave height to a maxima of approximately 1.8 meters, the turbulence dissipation rates for both sensors six and seven gradually approached values slightly greater than those visible for

day 110.5 (Figure 24).

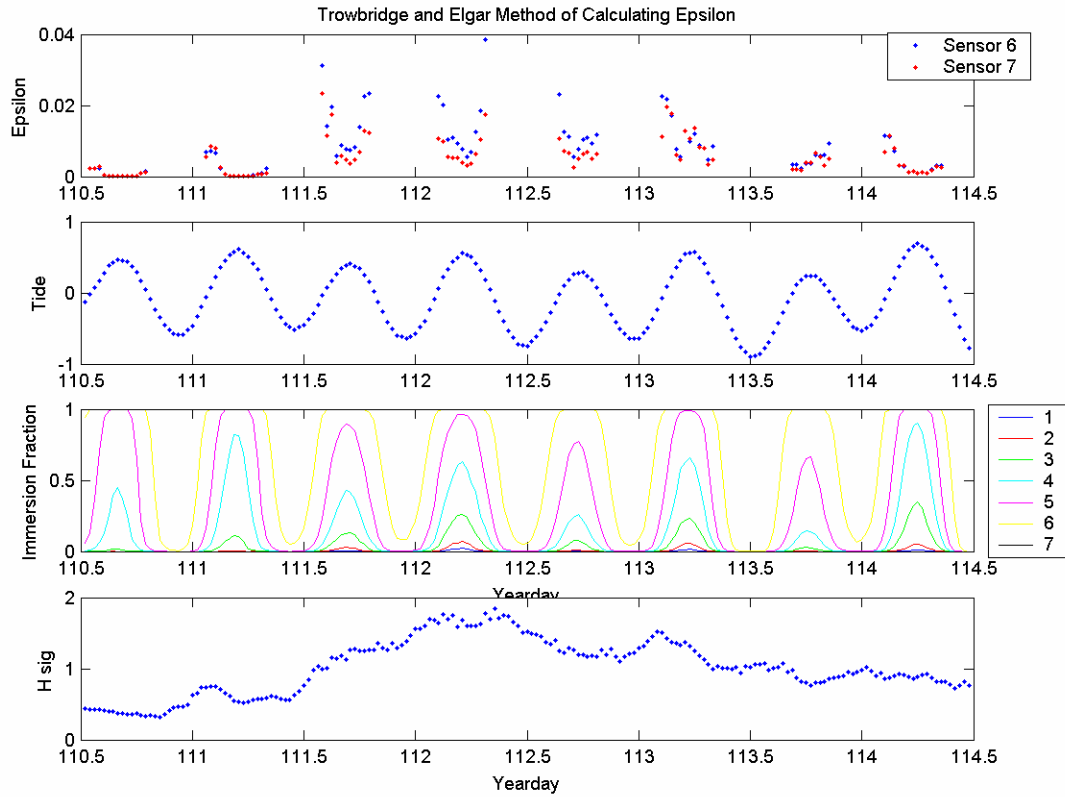


**Figure 24.** Turbulence dissipation rates for sensors six and seven (m<sup>2</sup>/s<sup>2</sup>) (top panel) using the criteria of a .95 sensor immersion; also included are the tide (m), (2nd panel from top), immersion fraction (2nd panel from the bottom) and the significant wave height, (m) (bottom panel).

The dissipation rates for sensor six and seven, correlated with water depth, as water depth decreased the turbulence dissipation rate increased (Figure 25).

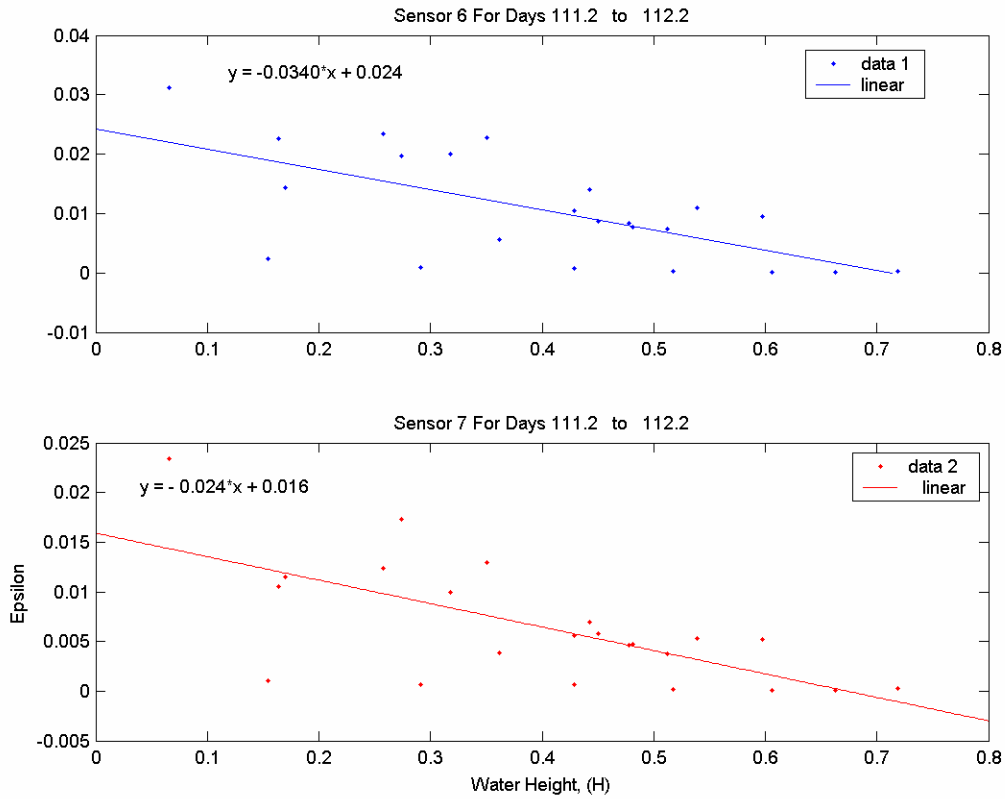


**Figure 25. Water depth (H) as compared to the dissipation rate of turbulence ( $\text{m}^2/\text{s}^2$ ) for day 111.2 to 112.2.**

Bore phased averaged mean currents, surface elevation and dissipation rates are shown in Figures 27 -30 for high tide at four successive days. Over the course of the ensemble bore cycle both the EM u and v horizontal component velocities grew. However, the horizontal velocity components decreased during the beginning of segment one and the end of segment ten, to the peaks in wave height. The magnitude of the horizontal u component velocity was much larger in comparison to the horizontal v component velocity under each bore segment and for each day studied. The EM u, cross-shore component velocity recorded velocities just over 1 meter per second, compared to the v alongshore component velocity, which at its greatest speed averaged under 0.05 meters per second; the negative values for both the u and v component velocities indicating the currents direction to be traveling onshore (Figures 26 27, 28 and 29). In addition, sensor six's current velocities were consistently equal or greater to those of sensor seven, for all periods of wave forcing

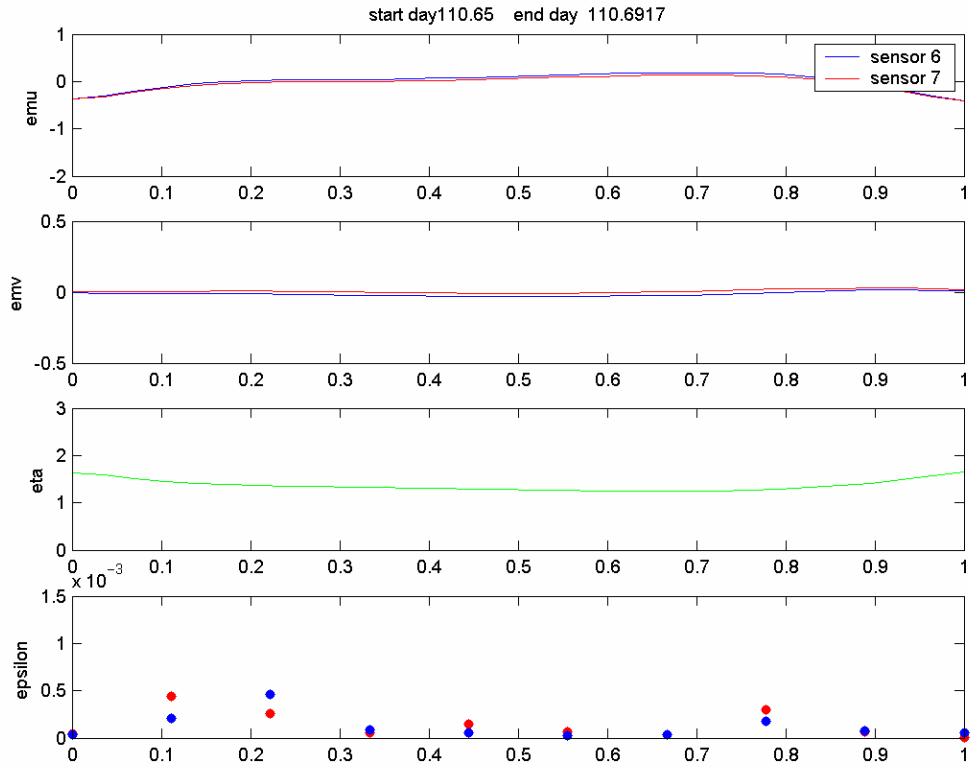


**Figure 26.** Borephase thirty minute ensemble averages of cross-shore current velocity (m/s) (top panel), alongshore current velocity (m/s) (2<sup>nd</sup> from top), sea surface elevation (m) (2<sup>nd</sup> from bottom) and dissipation rates ( $\text{m}^2/\text{s}^2$ ) (bottom panel) for sensors six and seven for day 110.65 to 110.6917, a period of low wave forcing.

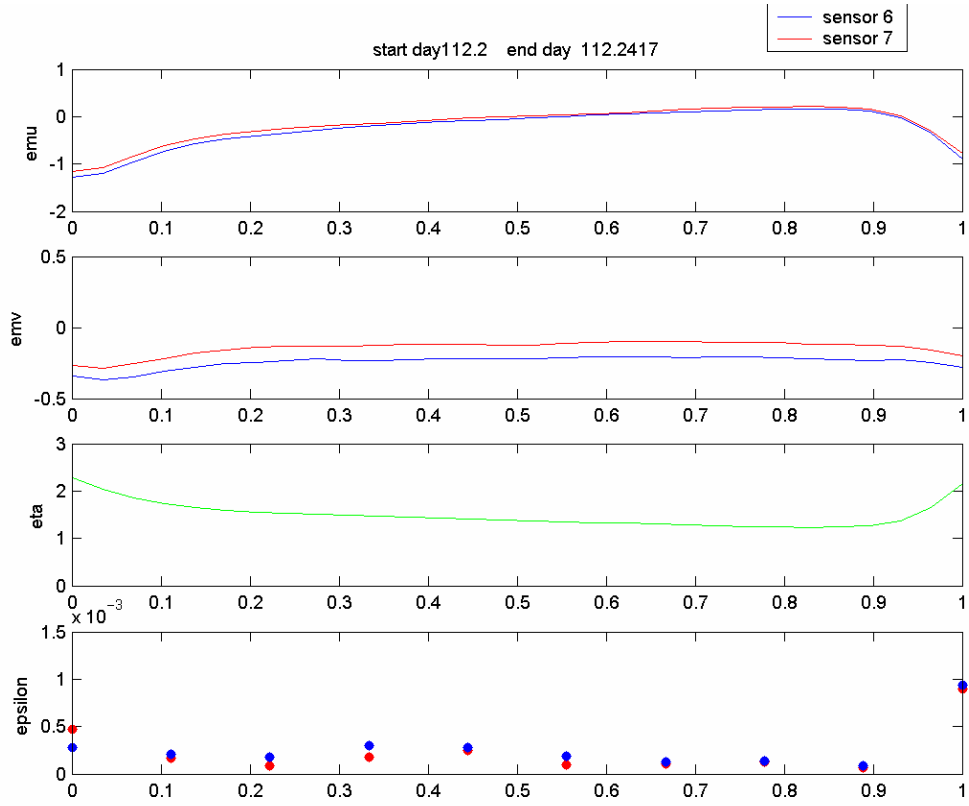


**Figure 27.** Borephase thirty minute ensemble averages of cross-shore current velocity (m/s) (top panel), alongshore current velocity (m/s) ( 2<sup>nd</sup> from top ), sea surface elevation (m) (2<sup>nd</sup> from bottom) and dissipation rates ( $\text{m}^2/\text{s}^2$ ) (bottom panel) for sensors six and seven for day 112.2 to 112.2417, a period of high wave forcing.

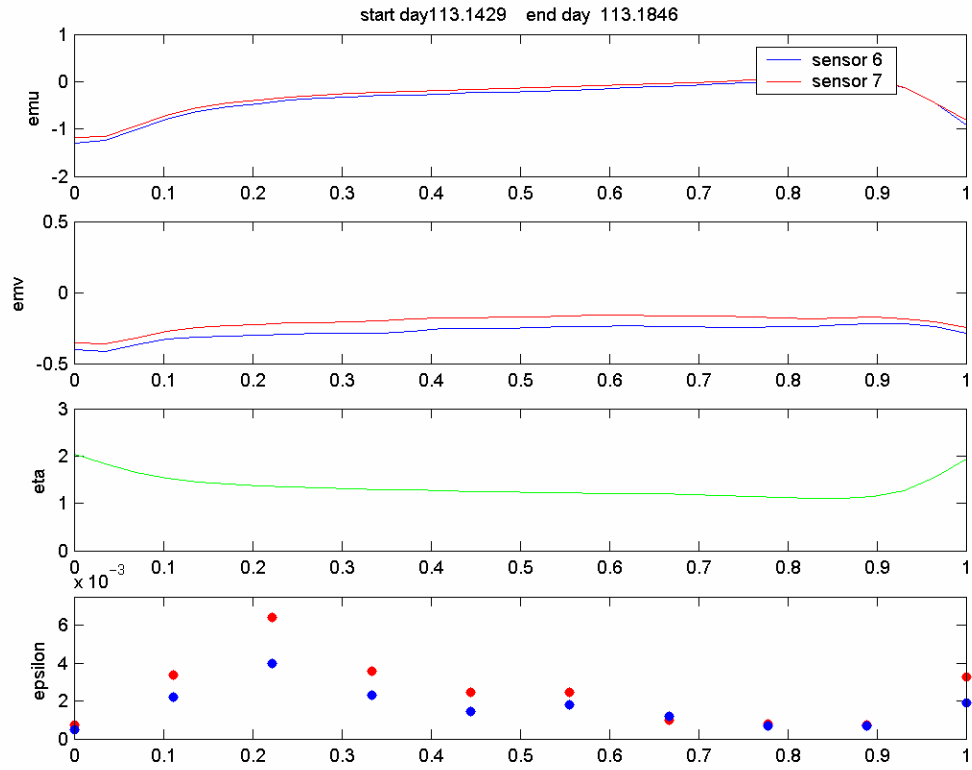


**Figure 28.** Borephase thirty minute ensemble averages of cross-shore current velocity (m/s) (top panel), alongshore current velocity (m/s) ( 2<sup>nd</sup> from top ), sea surface elevation (m) (2<sup>nd</sup> from bottom) and dissipation rates ( $\text{m}^2/\text{s}^2$ ) (bottom panel) for sensors six and seven for day 113.1429 to 113.1846, a period of moderate wave forcing. Note a change in the scaling of the dissipation rates in the bottom panel as compared to the other days in the series.



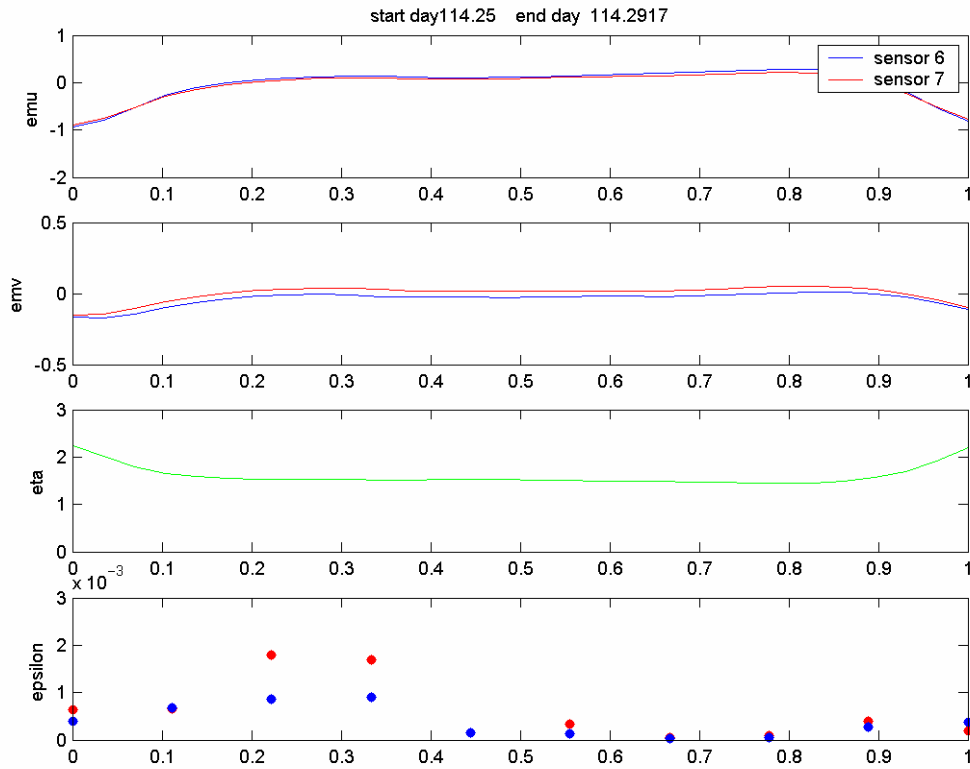


**Figure 29.** Borephase thirty minute ensemble averages of cross-shore current velocity (m/s) (top panel), alongshore current velocity (m/s) (2<sup>nd</sup> from top), sea surface elevation (m) (2<sup>nd</sup> from bottom) and dissipation rates (m<sup>2</sup>/s<sup>2</sup>) (bottom panel) for sensors six for day 114.25 to 114.2917, a period of moderate wave forcing. Note a change in scaling of dissipation rates as compared to other plots in the data series.

Examining the thirty minute ensemble averages for the rate of turbulence dissipation underneath the resolved bore segments, on average sensor six's rates of dissipation were larger than those of sensor seven. A notable exception occurred on day 113.1429 (Figure 28). Sensor seven's dissipation rate was consistently larger than that of sensor six's for the first half of the bore cycle, a possible result of increased bed shear stresses occurring below sensor seven. The highest rates of turbulence dissipation occurred in bore segments two and three for all four time intervals. As the peak of the bore occurred at the beginning of segment one, there was a lag in the increased rate of turbulence dissipation. This lag is most clearly demonstrated in Figures 28 and 29, during moderate wave forcing. Dissipation rates under segments two and three are two to six times greater than those in both the prior and preceding segments. The lowest rates of

dissipation in the bore cycle were shown to occur after the bore trough, possibly reflecting the advection time for the turbulence to reach the bed after wave breaking. The period of high wave forcing on day 112.2 appeared almost anomalous (Figure 27). Periods of moderate wave forcing following the rise in significant wave height produced dissipation rates significantly much greater. In comparison, a period of low energy wave forcing beginning at day 110.65 produced smaller rates of dissipation, and not substantially smaller than day 112.2's, (Figures 26 and 27).

The calculated dissipation rates by ensemble averaging over the entire data series yielded epsilon values that were orders of magnitudes greater than those calculated by the phase averaged bore analysis. Dissipation rates for ensemble wave averaging yield values which reached  $0.04 \text{ (m}^2\text{/s)}$  as seen in Figure 24. However, the turbulence dissipation rates by the phase averaged bore analysis only reached approximately  $0.006 \text{ m}^2\text{/s}$ . The reason for this difference is being investigated.

## V. CONCLUSIONS

In examining video imaging the surf zone boundary variations through video imaging techniques, it is evident that the tide is most important in determining surf zone breadth and distance in the cross-shore from the shoreline. As the tide lowers, the surf zone is shown to migrate away from the beach, and conversely at high tide the surf zone returns closer to shore.

Dissipation rates within a bore cycle were found to lag the peak of the bore with maximum dissipation 20-30 percent of the period after the peak. Cross-shore and alongshore current velocities underneath the bore were shown to increase over the bore cycle and decrease upon reaching a bore peak.

Using a method similar to the one by Trowbridge and Elgar (2001), in which horizontal velocity spectra are ensemble averaged over an entire thirty minute intervals, yielded dissipation rates that were orders of magnitude greater than those calculated through bore resolution techniques. Periods of highest significant wave forcing did not always result in the largest dissipation rates with the surf zone.

A recommended future area of study in examining the RIPEX dataset and turbulence dissipation is an examination of turbulence dissipation rates using a variation on the method prescribed by Thornton in his 1979 experiment. Using the vertical velocities recorded by the one sensor array on the RIPEX tower one may compare this method of separating and determining turbulence dissipation rates to those explored in this thesis.

THIS PAGE INTENTIONALLY LEFT BLANK

## LIST OF REFERENCES

Baker, M A., and C. H. Gibson, Sampling turbulence in the stratified ocean: statistical consequences of strong intermittency, *Journal of Physical Oceanography*, 17, 1817-1836, 1987.

Cox, D. T., and N. Kobayashi, A Kinematic Undertow Model with a Logarithmic Boundary Layer, *J. Wtury., Port, Coast. and Oc. Engrg.*, ASCE, 123, No. 6, pp. 354-360, 1997.

Faria, A. F. Garcez, E. B. Thornton, T.P. Stanton, C.V. Soares, T.C. Lippmann, Vertical profiles of longshore currents and related bed shear stress and bottom roughness, *Journal of Geophysical Research*, 103, C2, 3217-3232, 1998

George, R, R.E. Flick, R.T. Guza, Observations of Turbulence in the Surf Zone, *Journal of Geophysical Research*, 99 C1, 801-810, 1994.

Herbers, T.H.C and R.T. Guza, Comment on “Velocity Observations above a Rippled Bed using laser Doppler velocimetry” by Y.C. Agrawal and D.G. Aubrey, *Journal of Geophysical Research*, 98, C11, 20331-20333, 1993.

Kundu, P.K. Fluid Mechanics, Academic Press, Inc., 1990.

Lumley, J.L. and E.A. Terray, Kinematics of Turbulence Convected by a Random Wave Field, *Journal of Physical Oceanography*, 13, 2000-2007, 1983.

MacMahan, J. H, E. B. Thornton, T. P. Stanton, A J.H.M Reniers, RIPEX: Observations of a rip current system, *Marine Geology*, 218 (1-4) 113-134, 2005.

Stanton, T.P., [www.oc.nps.navy.mil/riplex/instruments/index.htm](http://www.oc.nps.navy.mil/riplex/instruments/index.htm), 2002.

Stanton, T.P., and E. B. Thornton., [www.oc.nps.navy.mil/riplex2/proposal/riplex.htm](http://www.oc.nps.navy.mil/riplex2/proposal/riplex.htm) 2002, a.

Stanton, T.P., and EB. Thornton., [www.oc.nps.navy.mil/riplex/sbe2/summary/steep.htm](http://www.oc.nps.navy.mil/riplex/sbe2/summary/steep.htm), 2002, b.

Tennekes, H. and J.L. Lumley. A First Course in Turbulence, The MIT Press, pp 183-196, 1972.

Thornton, E. B., Energetics of breaking waves within the surf zone, *Journal of Geophysical Research*, 84, C8, 4931-4938, 1979.

Trowbridge, J. and S. Elgar, Turbulence measurements in the surf zone, *Journal of Physical Oceanography*, 31, 2403-2417, 2001.

THIS PAGE INTENTIONALLY LEFT BLANK

## INITIAL DISTRIBUTION LIST

1. Defense Technical Information Center  
Ft. Belvoir, VA
2. Dudley Knox Library  
Naval Postgraduate School  
Monterey, CA
3. Professor Edward B. Thornton  
Naval Postgraduate School  
Monterey, CA
4. Professor Timothy P. Stanton  
Naval Postgraduate School  
Monterey, CA
5. Professor Donald P. Brutzman  
Naval Postgraduate School  
Monterey, CA
6. Professor Mary L. Batteen  
Naval Postgraduate School  
Monterey, CA